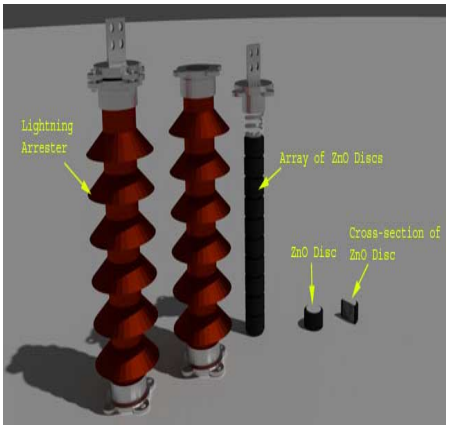

Chapter 7

Electrical and Structural Characterization of ZrO_2 doped ZnO – V_2O_5 – Cr_2O_3 Varistor Ceramics Sintered at Different Temperatures.

Chapter 7

Electrical and Structural Characterization of ZrO_2 doped $ZnO–V_2O_5–Cr_2O_3$ Varistor Ceramics Sintered at Different Temperatures.

This chapter addresses the effect of ZrO_2 doping on electrical and strutural properties of $ZnO–V_2O_5–Cr_2O_3$ based varistors. The current chapter is divided into following two sections: -

Section 1: This section of the chapter describes synthesis of ZrO_2 doped $ZnO–V_2O_5–Cr_2O_3$ varistor ceramics sintered at 850°C, 900°C and 950°C and their structural characterization using XRD, SEM and EDS.

Section 2: This section discusses the influence of the grain boundaries structure on the electrical properties of ZnO based ceramics in a systematic manner using AC impedance and dieclctric spectroscopy (IS). Various properties investigated include grain boundary resistance, dielectric constant (ε'), tan δ, non-linear coefficent, breakdown field, leakage current density and breakdown voltage per grain boundary.

Overview: ZrO_2 characterized by high hardness, better wearing quality and longer service life, can largely reduce the waste of material grinding. Kim et al. [12] studied microstructure and electrical properties of ZnO varistor ceramics under different ZrO_2 content and the sintering temperature. Doping with certain ZrO_2 improved comprehensive electrical properties of ZnO varistor ceramics. Considering that little research works of modifying the ZnO varistor ceramics by doping with ZrO_2 have even been done, furthermore, Zr^{4+} ion (0.080 nm) is close to Zn^{2+} ion (0.074 nm) and doping with certain ZrO_2 is very likely to exhibit unique advantages of ZnO varistor ceramics, the present work focus on the experimental investigations of the effect of ZrO_2 doping on the microstructure and electrical properties by a solid reaction route. Effects of various ZrO_2 content doping on the microstructure and the influence of the grain boundary behaviour on the electrical properties of the ZnO varistor ceramics were investigated and

some new results were obtained, which supply some theoretical foundation for ZrO_2-doped ZnO varistor ceramics.

7.1. Synthesis and Structural Behavior of ZrO_2 Doped ZnO–V_2O_5–Cr_2O_3 Varistor Ceramics.

Reagent grade high purity Sigma Aldrich: ZnO (> 99.00%), V_2O_5 (99.60%), Cr_2O_3 (99.50%) and ZrO_2 (99.90%) were used as raw materials. To investigate the effect of ZrO_2 addition Five compositions (96.5 - x) mol% ZnO + 0.5 mol% V_2O_5 + 3.0 mol% Cr_2O_3 + x – mol% ZrO_2 (where x = 0.00, 0.10, 0.50, 1.00 and 2.00) were prepared using solid state reaction. The compositions chosen and the sintering conditions used for each varistor composition are summarized in Tables 7.1, 7.2 and 7.3. All the compositions were mixed homogeneously by conventional ball milling using zirconia balls in acetone in a poly-propylene bottle for 24 h. Thereafter, the mixtures were filtered, dried and calcined at 650 °C for 3 h. The agglomerates were pulverized using an agate mortar-pestle followed by uniaxially pressed into pellets having approximately diameters of 12 mm and thickness 1 mm in a hydraulic press at a pressure of 150 MPa using polyvinyl butyral (PVB) as a binder. The pellets were covered with raw powder and placed inside a closed double alumina crucible at different sintering temperature 850 °C, 900 °C and 950 °C respectively for a soaking period of 3 h with both heating and cooling rate of 3 °C/min. Before electrical measurements, the sintered pellets were polished with emery paper on both the sides and then annealed at 700 °C for 5 h to stabilize the electrical properties. High temperature conductive silver paste was used to coat both faces of the pellets and the electrodes were formed by curing the paste at 600 °C for 10 min.

A **nomenclature** e.g. 850CZ100 is given to each sample. Here '850' denote the sintering temperature in °C, 'C' denotes Cr_2O_3, 'Z' denotes ZrO_2, '100' denotes the mole percent of ZrO_2 as 1.0 mol%. Tables 7.1, 7.2 and 7.3 shows the nomenclature of samples.

Table 7.1: Summary of samples composition and their nomenclature, sintered density 'ρ' and average grain size for samples sintered at 850 °C for 3 h.

Sample nomenclature	Composition (mol%): Sintered at 850°C for 3 h				Sintered density (gm/cc)	Average grain size (μm)
	ZnO	V_2O_5	Cr_2O_3	ZrO_2		
850CZ000	96.5	0.50	3.00	0.00	5.32	2.4
850CZ010	96.4	0.50	3.00	0.10	5.33	1.7
850CZ050	96.0	0.50	3.00	0.50	5.31	2.1
850CZ100	95.5	0.50	3.00	1.00	5.33	1.3
850CZ200	94.5	0.50	3.00	2.00	5.33	1.1

Table 7.2: Summary of samples composition and their nomenclature, sintered density 'ρ' and average grain size for samples sintered at 900 °C for 3 h.

Sample nomenclature	Composition (mol%): Sintered at 900°C for 3 h				Sintered density (gm/cc)	Average grain size (μm)
	ZnO	V_2O_5	Cr_2O_3	ZrO_2		
900CZ000	96.5	0.50	3.00	0.00	5.48	3.8
900CZ010	96.4	0.50	3.00	0.10	5.47	3.1
900CZ050	96.0	0.50	3.00	0.50	5.46	2.6
900CZ100	95.5	0.50	3.00	1.00	5.46	1.7
900CZ200	94.5	0.50	3.00	2.00	5.47	1.4

Table 7.3: Summary of samples composition and their nomenclature, sintered density 'ρ' and average grain size for samples sintered at 950 °C for 3 h.

Sample nomenclature	Composition (mol%): Sintered at 950°C for 3 h				Sintered density (gm/cc)	Average grain size (μm)
	ZnO	V_2O_5	Cr_2O_3	ZrO_2		
950CZ000	96.5	0.50	3.00	0.00	5.49	4.1
950CZ010	96.4	0.50	3.00	0.10	5.49	3.5
950CZ050	96.0	0.50	3.00	0.50	5.49	4.5
950CZ100	95.5	0.50	3.00	1.00	5.47	2.2
950CZ200	94.5	0.50	3.00	2.00	5.49	2.5

7.1.1. X-Ray Diffraction (XRD)

The strong and sharp diffraction peaks of the XRD patterns of ZnO varistors sintered at temperature 850 °C, 900 °C and 950 °C are shown in Figs. 7.1, 7.2 and 7.3 respectively and demonstrate that the products are well crystalline. Diffraction peaks present in the XRD patterns of different specimens were matched with the XRD - JCPDS files of constituent phases and other compounds which might have formed during sintering. It has been found that peaks in the XRD patterns matched with JCPDS files of hexagonal ZnO (file no. 361451). Crystallite size of different phases was calculated from the measurement of FWHM of XRD peaks of different phases using Scherer formula. From the calculated values, it can be found that the crystallite size lies in the range of 49-69 nm.

Fig. 7.1 shows XRD patterns of the 0.00, 0.10, 0.50, 1.00 and 2.00 mol% ZrO_2 doped ZnO–V_2O_5–Cr_2O_3 varistor samples sintered at 850 °C for 3 h. For all of the samples doped with ZrO_2, Apart from the major ZnO phase, $Zn_3(VO_4)_2$ (JCPDS card no. 191470, 191468 and 340378), $ZnCr_2O_4$ (JCPDS card no. 221107) and ZrO_2 (JCPDS card no. 460046) were detected as minor secondary phases formed at the grain boundaries and the triple point junction. The secondary phases were produced by the following chemical reaction: $3ZnO + V_2O_5 \rightarrow Zn_3(VO_4)_2$.The major peaks could be indexed as reflections from planes (100), (002), (101), (102) and (110) of hexagonal ZnO. These were identified by comparing with standard JCPDS card no. 361451.The lattice parameters and the crystallite size for ZrO_2 doped ZnO varistor samples sintered at 850 °C is given in Table 7.4. The larger lattice parameters of ZrO_2 doped samples are due to the larger radii of Zr^{4+} ion (0.080 nm). With a radius greater than that of Zn^{2+} ion (0.074 nm), Zr^{4+} ions enter into the ZnO lattice, occupy the sites of Zn^{2+} ions and cause an expansion in the lattice parameter, and it is thought that Zr ions substitute for Zn ions. The peak positions of (002) for 0.00, 0.10, 0.50, 1.00 and 2.00 mol% ZrO_2 doped ZnO–V_2O_5–Cr_2O_3 varistor samples sintered at 850 °C are 34.53, 34.49, 34.48, 34.51 and 34.50 degree respectively (Table: 7.4). It can be observed from the data that with ZrO_2 doping the peak positions of (002) planes shift slightly

toward lower angle as compared to un-doped ZrO_2 sample. The crystallite size for the 0.00, 0.10, 0.50, 1.00 and 2.00 mol% ZrO_2 doped $ZnO–V_2O_5–Cr_2O_3$ varistor samples sintered at 850 °C are obtained as 49.1, 51.2, 53.1, 54.3 and 56.7 nm respectively are given in Table 7.4.

X-ray diffraction patterns of the 0.00, 0.10, 0.50, 1.00 and 2.00 mol% ZrO_2 doped $ZnO–V_2O_5–Cr_2O_3$ samples sintered at 900 °C for 3 h are shown in Fig. 7.2. For all of the samples doped with ZrO_2, Apart from the major ZnO phase, $Zn_3(VO_4)_2$ (JCPDS card no. 191470, 191468 and 340378), $ZnCr_2O_4$ (JCPDS card no. 221107) and ZrO_2 (JCPDS card no. 460046) were detected as minor secondary phases formed at the grain boundaries and the triple point junction. The formation of the $ZnCr_2O_4$ spinel phase is often reported in Bi_2O_3-doped ZnO varistor systems containing Cr_2O_3. The V_2O_5 additives can enhance the densification and grain growth behaviour of the $ZnO–V_2O_5$ materials due to the formation of $Zn_3(VO_4)_2$, which acts as a liquid-phase sintering aid at high temperature. The major peaks could be indexed as reflections from planes (100), (002), (101), (102) and (110) of hexagonal ZnO. These were identified by comparing with standard JCPDS card no. 361451.The lattice parameters and the crystallite size for ZrO_2 doped ZnO varistor samples sintered at 900 °C is given in Table 7.5.

The peak positions of (002) for 0.00, 0.10, 0.50, 1.00 and 2.00 mol% ZrO_2 doped $ZnO–V_2O_5–Cr_2O_3$ varistor samples sintered at 900 °C are 34.50, 34.49, 34.48, 34.51 and 34.49 degree respectively (Table: 7.5). It can be observed from the data that with ZrO_2 doping the peak positions of (002) planes shift slightly as compared to un-doped ZrO_2 sample. The crystallite size for the 0.00, 0.10, 0.50, 1.00 and 2.00 mol% ZrO_2 doped $ZnO–V_2O_5–Cr_2O_3$ varistor samples sintered at 900 °C are obtained as 57.3, 56.9, 55.5, 48.7 and 45.8 nm respectively are given in Table 7.5.

Table 7.4: Lattice parameters, percentage theoretical density (T.D) and crystallite size D (nm) for (002) of ZrO_2 doped samples sintered at 850 °C.

Sample Name	a=b (A°)	c (A°)	Unit cell volume (A°^{3})	% theoretical density (T.D)	Crystallite size D (nm)	2θ° for (002)
850CZ000	3.248	5.204	47.558	93.76	49.1	34.53
850CZ010	3.248	5.202	47.526	93.72	51.2	34.49
850CZ050	3.247	5.203	47.527	93.37	53.1	34.48
850CZ100	3.248	5.207	47.591	93.84	54.3	34.51
850CZ200	3.249	5.209	47.618	93.89	56.7	34.50

Table 7.5: Lattice parameters, percentage theoretical density (T.D) and crystallite size D (nm) for (002) of ZrO_2 doped samples sintered at 900 °C.

Sample Name	a = b (A°)	c (A°)	Unit cell volume (A°^{3})	% theoretical density (T.D)	Crystallite size D (nm)	2θ° for (002)
900CZ000	3.249	5.209	47.63	96.55	57.3	34.50
900CZ010	3.248	5.205	47.56	96.24	56.9	34.49
900CZ050	3.248	5.203	47.55	96.06	55.5	34.48
900CZ100	3.249	5.205	47.58	96.12	48.7	34.51
900CZ200	3.249	5.206	47.61	96.34	45.8	34.49

Table 7.6: Lattice parameters, percentage theoretical density (T.D) and crystallite size D (nm) for (002) of ZrO_2 doped samples sintered at 950 °C.

Sample Name	a = b (Aº)	c (Aº)	Unit cell volume (Aº^3)	% theoretical density (T.D)	Crystallite size D (nm) for (002)	2θ° for (002)
950CZ000	3.251	5.209	47.68	96.98	58.5	34.45
950CZ010	3.245	5.201	47.43	96.33	60.2	34.45
950CZ050	3.248	5.204	47.54	96.56	62.3	34.48
950CZ100	3.249	5.203	47.56	96.25	57.3	34.49
950CZ200	3.249	5.206	47.60	96.67	68.5	34.49

Fig. 7.3 shows X-ray diffraction patterns of the 0.00, 0.10, 0.50, 1.00 and 2.00 mol% ZrO_2 doped ZnO–V_2O_5–Cr_2O_3 samples sintered at 950 °C for 3 h are shown in Fig. 7.3. For all of the samples doped with ZrO_2, Apart from the major ZnO phase, $Zn_3(VO_4)_2$ (JCPDS card no. 191470, 191468 and 340378), $ZnCr_2O_4$ (JCPDS card no. 221107) and ZrO_2 (JCPDS card no. 460046) were detected as minor secondary phases formed at the grain boundaries and the triple point junction. The secondary phases were produced by the following chemical reaction: $3ZnO + V_2O_5 \rightarrow Zn_3(VO_4)_2$.

The major peaks could be indexed as reflections from planes (100), (002), (101), (102) and (110) of hexagonal ZnO. These were identified by comparing with standard JCPDS card no. 361451.The lattice parameters and the crystallite size for ZrO_2 doped ZnO varistor samples sintered at 950 °C is given in Table 7.6.

The peak positions of (002) for 0.00, 0.10, 0.50, 1.00 and 2.00 mol% ZrO_2 doped ZnO–V_2O_5–Cr_2O_3 varistor samples sintered at 950 ºC are 34.45, 34.45, 34.48, 34.49 and 34.49 degree respectively (Table: 7.6). It can be observed from the data that with ZrO_2 doping the peak positions of (002) planes shift slightly toward higher angle as compared to un-doped ZrO_2 sample. The crystallite size for the 0.00, 0.10, 0.50, 1.00 and 2.00 mol% ZrO_2 doped ZnO–V_2O_5–Cr_2O_3 varistor samples sintered at 950 °C are obtained as 58.5, 60.2, 62.3, 57.3 and 68.5 nm respectively are given in Table 7.6.

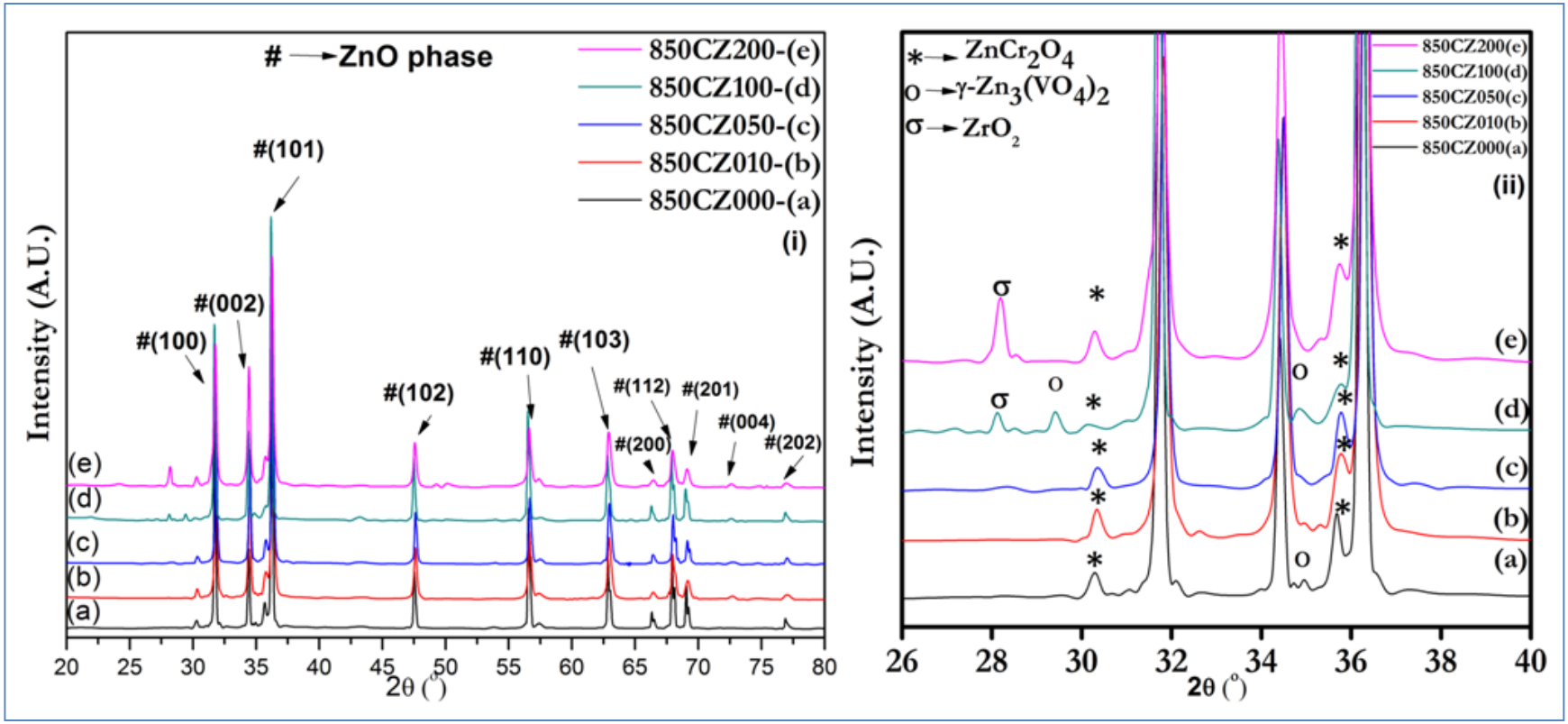

Figure 7.1: X-ray diffraction patterns of samples sintered at 850 °C with following compositions: (a) 850CZ000 (0.00 mol% ZrO_2); (b) 850CZ010 (0.10 mol% ZrO_2); (c) 850CZ050 (0.50 mol% ZrO_2); (d) 850CZ100 (1.00 mol% ZrO_2) and (e) 850CZ200 (2.00 mol% ZrO_2)

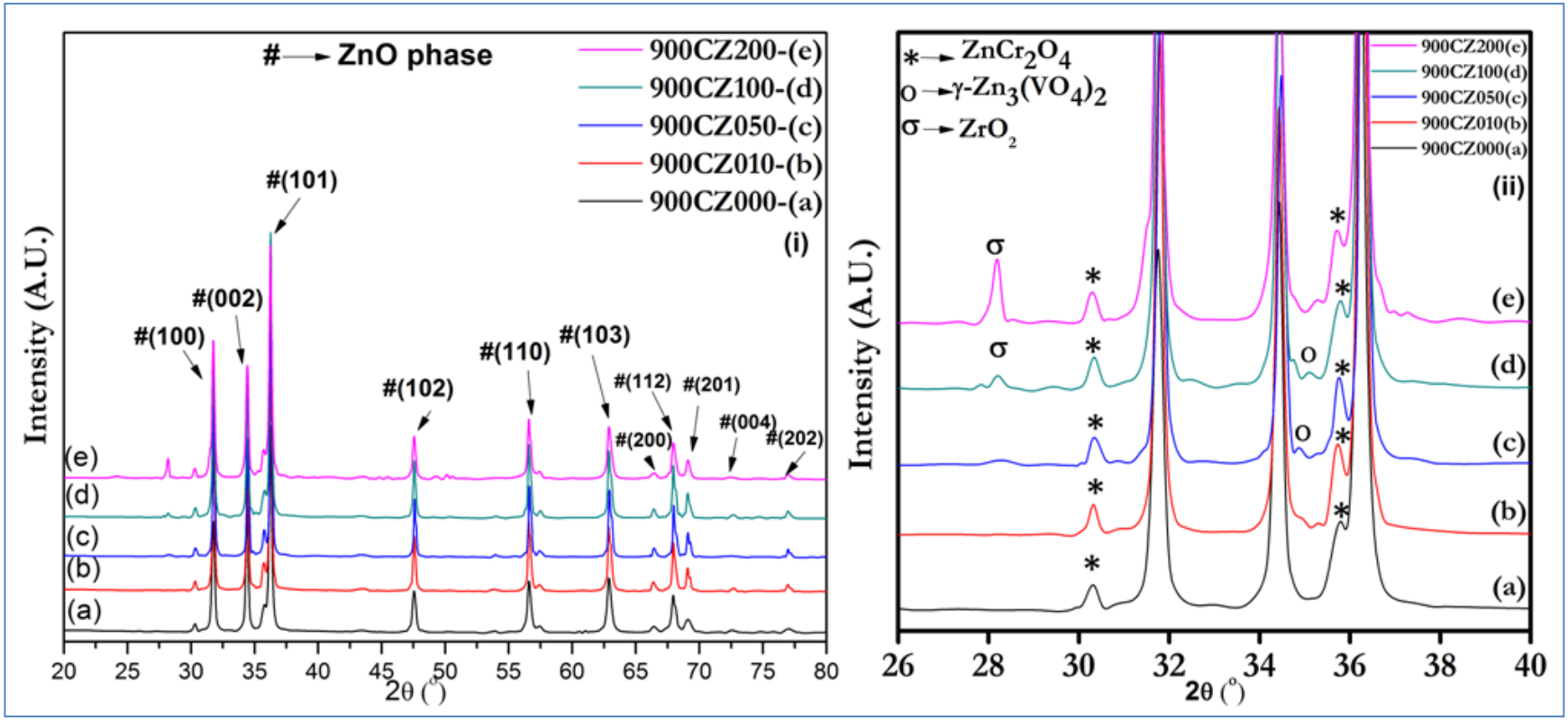

Figure 7.2: X-ray diffraction patterns of samples sintered at 900 °C with following compositions: (a) 900CZ000 (0.00 mol% ZrO_2); (b) 900CZ010 (0.10 mol% ZrO_2); (c) 900CZ050 (0.50 mol% ZrO_2); (d) 900CZ100 (1.00 mol% ZrO_2) and (e) 900CZ200 (2.00 mol% ZrO_2)

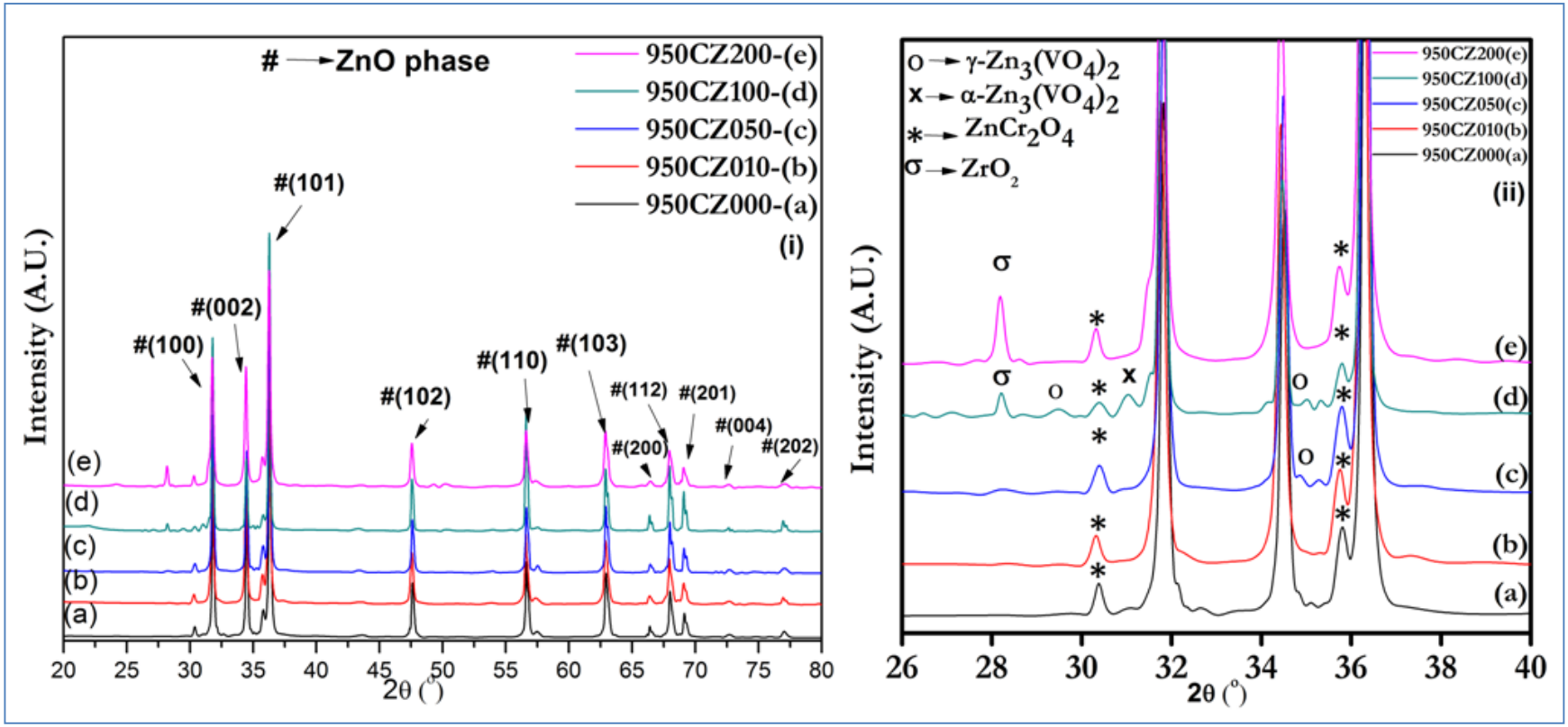

Figure 7.3: X-ray diffraction patterns of samples sintered at 950 °C with following compositions: (a) 950CZ000 (0.00 mol% ZrO_2); (b) 950CZ010 (0.10 mol% ZrO_2); (c) 950CZ050 (0.50 mol% ZrO_2); (d) 950CZ100 (1.00 mol% ZrO_2) and (e) 950CZ200 (2.00 mol% ZrO_2)

7.1.2. Scanning Electron Microscopy (SEM)

Figs. 7.4 shows the SEM micrographs of the chemically etched samples sintered at 850 °C for 0.00, 0.10, 0.50, 1.00 and 2.00 mol% ZrO_2 doped ZnO–V_2O_5–Cr_2O_3 samples. Grain size are calculated as 2.4, 1.7, 2.1, 1.3 and 1.1 μm respectively from SEM micrographs. Small, closely spaced anhedral grains were nonuniformly distributed across the sample. Since the eutectic temperature for V_2O_5-ZnO is approximately 600°C, a liquid phase sintering process occurs when the sintering temperature is higher than the eutectic temperature that's lead to grain growth of ZnO and to densification of sample. For the samples sintered at 850 °C, the overall trend in the grain growth decreases with increase of ZrO_2 doping concentration. This indicates that ZrO_2 acts as a grain growth inhibitors. The sample microstructure shown in Figs. 7.4 (a–e) was quite dense, with areas of closed spherical porosity, indicating the sintering process had reached to the final stage. Anisotropic grain growth results from sintering in the presence of a liquid phase. Overall, it can be seen that the grain size is inhomogeneous, despite clear grain boundaries. The average grain size of the 0.00 mol% ZrO_2 system was found to be 2.4 μm, which decreased to 1.7 μm by addition of 0.00 mol% ZrO_2 . Further addition of ZrO_2 decreased the average grain size to 1.1 μm. The sample doped with 1.00 mol% ZrO_2 exhibited the most uniform grain size of 1.3 μm. For the samples sintered at 850°C, the overall trend in the grain growth decreases with the increase of ZrO_2 doping level.

Figs. 7.5 shows the SEM micrographs of the chemically etched samples sintered at 900 °C for 0.00, 0.10, 0.50, 1.00 and 2.00 mol% ZrO_2 doped ZnO–V_2O_5–Cr_2O_3. Grain size of 3.8, 3.1, 2.6, 1.7 and 1.4 μm respectively are caculated from SEM micrographs. Microstructures at low magnification show a dense phase micrograph with small amount of porosity indicating that the sintering process had reached the final stage. Anisotropic grain growth observed resulting from sintering in the presence of a liquid phase. For the samples sintered at 900°C, the average grain size of the 0.00 mol% ZrO_2 system was found to be 3.8 μm, which first decresed to 1.4 μm by addition of 2.00 mol% ZrO_2. The sample doped with 0.50 mol% ZrO_2 exhibited the most

uniform grain size. The addition of mol% ZrO_2 saw an decrease in the ZnO grain size. The results suggest that the addition of ZrO_2 has a beneficial effect in suppressing the exaggerated ZnO grain growth that is often. observed in ZnO–V_2O_5 systems, and it is an effective grain growth inhibitor. Fig. 7.7 shows the SEM micrographs of the fractured samples sintered at 900 °C.

SEM micrographs of the chemically etched samples sintered at 950 °C for 0.00, 0.10, 0.50, 1.00 and 2.00 mol% ZrO_2 doped ZnO–V_2O_5–Cr_2O_3 samples are shown in Figs. 7.6. Grain size are calculated as 4.1, 3.5, 4.5, 2.2 and 2.5 μm respectively from SEM micrograph. Microstructures at low magnification show a dense phase micrograph with areas of the closed spherical porosity indicating that the sintering process had reached to the final stage. Anisotropic grain growth obsered resulting from sintering in the presence of a liquid phase. For the samples sintered at 950 °C. The average grain size of the 0.0 mol% ZrO_2 system was found to be 4.1 μm, which first decresed to 2.2 μm by addition of 1.0 mol% ZrO_2. Further addition of ZrO_2 (2.0 mol %) slightly increased the average grain size to 2.5 μm. The specimen with 1.00 mol% ZrO_2 exhibited the largest grain size of 2.2 μm among all the samples. The microstructure observation revealed that the ZrO_2 acts as a grain growth reducer. For ZrO_2 sample, ZrO_2 could precipitate with ZnO along the grain boundaries and participates in lowering the grain size of the Zr-doped samples. The XRD and SEM of the samples show the presence of ZrO_2. As the doping content increases, the grain size of ZnO decreases.

SEM micrographs of the samples at different ZrO_2 content show the following features: (i) the average grain size depends on the ZrO_2 doping, (ii) there were large grains dispersed in a matrix composed of small grains, (iii) the large grains grew faster than the small grains, (iv) the large grains always had an oblong shape and (v) the microstructure observation revealed that the ZrO_2 acts as a grain growth inhibitor. With respect to the oblong shape of exaggerated grains, it observed that the grain growth in these samples was quite anisotropic.

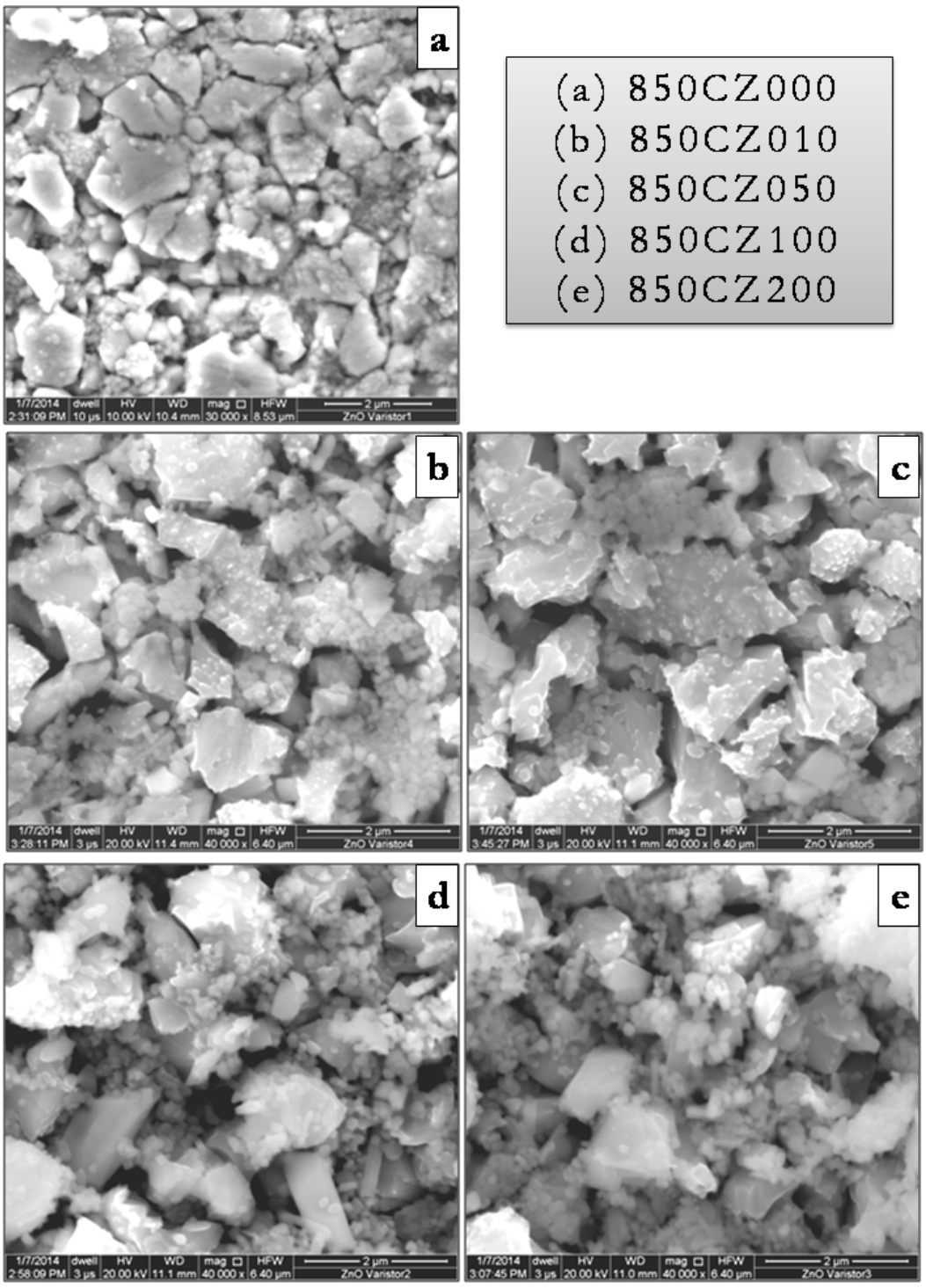

Figure 7.4: SEM micrographs of the sample sintered at 850 °C with following compositions: (a) 850CZ000 (0.00 mol% ZrO_2); (b) 850CZ010 (0.10 mol% ZrO_2); (c) 850CZ050 (0.50 mol% ZrO_2); (d) 850CZ100 (1.00 mol% ZrO_2) and (e) 850CZ200 (2.00 mol% ZrO_2)

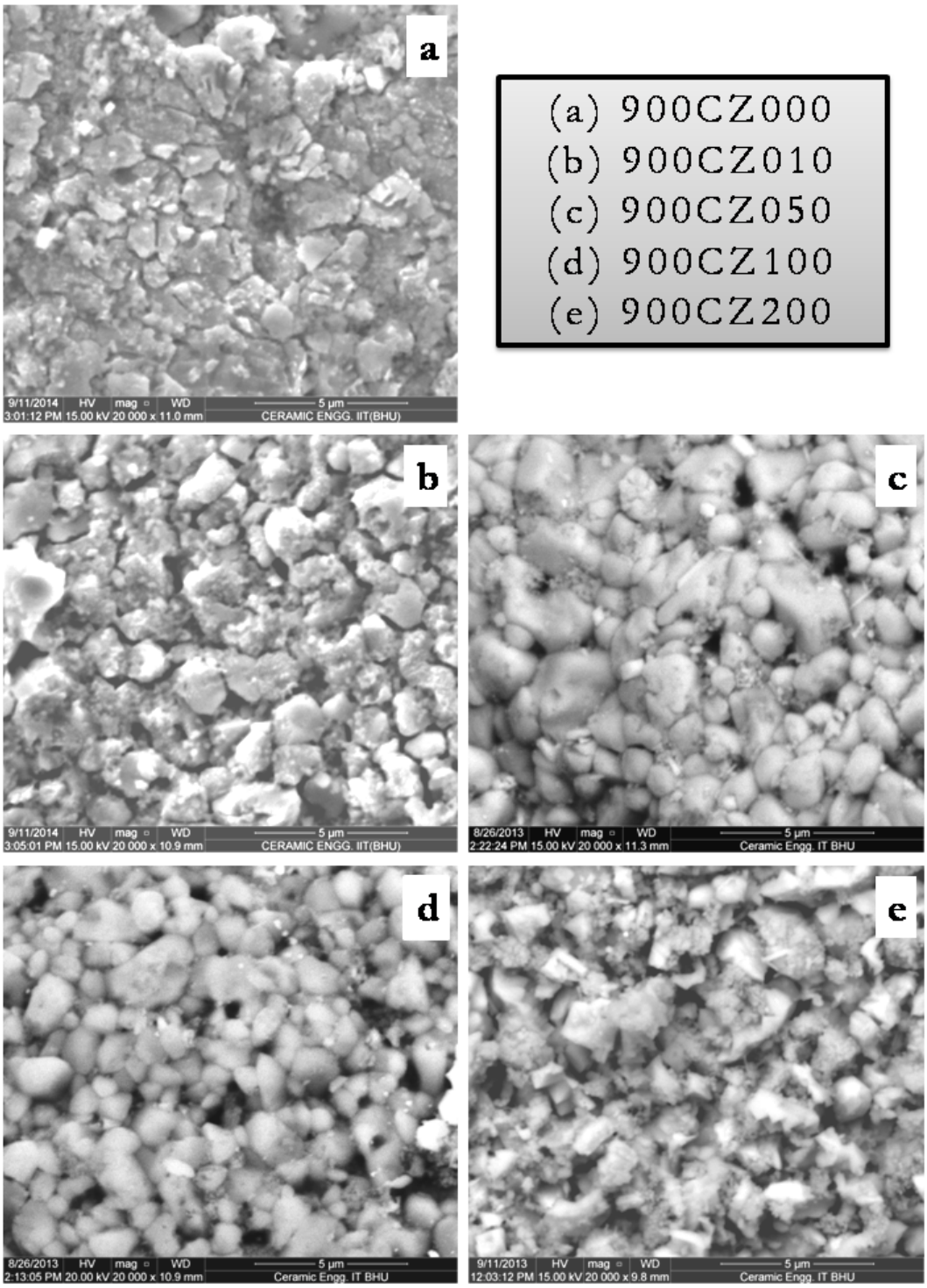

Figure 7.5: SEM micrographs of the sample sintered at 900 °C with following compositions: (a) 900CZ000 (0.00 mol% ZrO_2); (b) 900CZ010 (0.10 mol% ZrO_2); (c) 900CZ050 (0.50 mol% ZrO_2); (d) 900CZ100 (1.00 mol% ZrO_2) and (e) 900CZ200 (2.00 mol% ZrO_2)

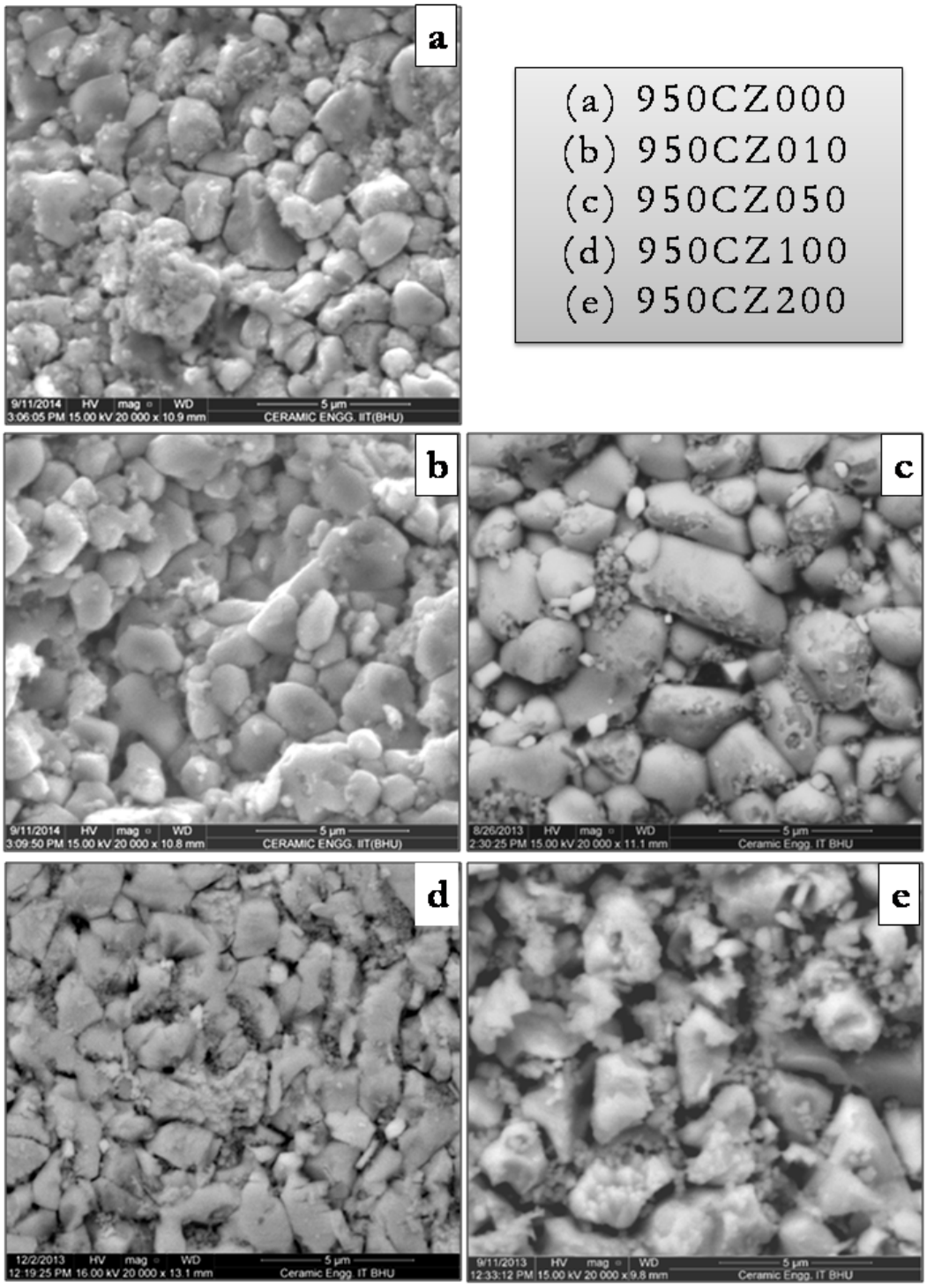

Figure 7.6: SEM micrographs of the sample sintered at 950 °C with following compositions: (a) 950CZ000 (0.00 mol% ZrO_2); (b) 950CZ010 (0.10 mol% ZrO_2); (c) 950CZ050 (0.50 mol% ZrO_2); (d) 950CZ100 (1.00 mol% ZrO_2) and (e) 950CZ200 (2.00 mol% ZrO_2)

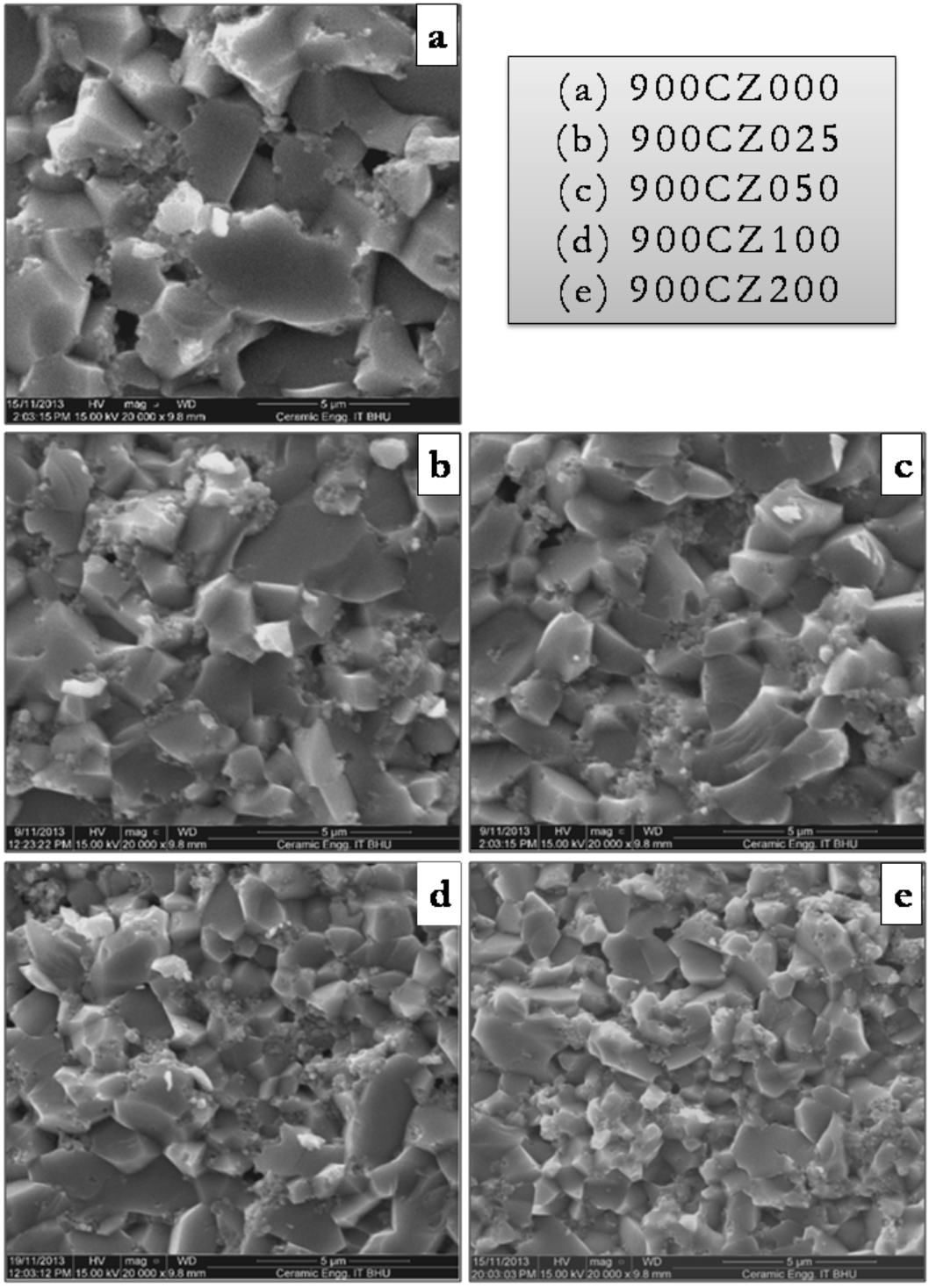

Figure 7.7: SEM micrographs of the fractured samples sintered at 900 °C with following compositions: (a) 900CZ000 (0.00 mol% ZrO_2); (b) 900CZ010 (0.10 mol% ZrO_2); (c) 900CZ050 (0.50 mol% ZrO_2); (d) 900CZ100 (1.00 mol% ZrO_2) and (e) 900CZ200 (2.00 mol% ZrO_2)

7.1.3. Energy-Dispersive X-Ray Spectroscopy (EDS)

EDS spectra for 0.10 mol% ZrO_2 doped ZnO–V_2O_5–Cr_2O_3 System (900CZ010) at different regions, especially grain interiors and grain boundaries, are shown in Fig. 7.8. EDS spectra of the ZnO grain boundary reveal V and Cr segregation in the sample 900CZ010. At triplet point, a secondary phase consists of Cr was confirmed by XRD and EDS spectra. Fig. 7.9 shows EDS elemental maps for Zn, O, V and Cr of samples with addition of 0.10 mol% ZrO_2, 3.00 mol% Cr_2O_3, 0.50 mol% V_2O_5 and 96.40 mol% ZnO.

EDS spectra for 1.00 mol% ZrO_2 doped ZnO–V_2O_5–Cr_2O_3 (900CZ100) sample (sintered at 900°C) at different regions, especially the grain interior and the grain boundary, are shown in Fig. 7.10 EDS spectra of the ZnO grain boundary shows V, Cr and Zr segregation in the sample (900CZ100). At lower concentration, ZrO_2 could precipitate together with ZnO along the grain boundaries and participates in lowering the grain size of the doped samples. Fig. 7.11 shows EDS elemental maps for Zn, O, V, Cr and Zr of samples with the addition of 1.00 mol% ZrO_2, 3.00 mol% Cr_2O_3, 0.50 mol%V_2O_5 and 95.50 mol% ZnO. The grey-scale density in the EDS elemental maps images increases with increasing amount of an element present. V is present at the grain boundaries and coexists with segregated particles, such as spinel particles $ZnCr_2O_4$ and the unknown compound at the triple points in the samples. The XRD and EDS analysis results reveal that V is incorporated in spinel particles.

EDS confirms that only Zn, O, Cr and Zr are present in the samples. The entire samples were observed to be oxygen deficient. The 0.10 mol% ZrO_2 doped ZnO–V_2O_5–Cr_2O_3 (900CZ010) sample sintered at 900°C was observed to be most oxygen deficient. The deficiency or excess of the constituent material results in distorted band structure with corresponding decrease in resistivity. Zinc oxide loses oxygen on heating so that the zinc is in excess. The oxygen of course evolves as electrically neutral substance so that it is associated with each excess zinc ion in the crystal; there will be two electrons that remain trapped in the solid material, thus leading to non-stoichiometricity in the solid. This leads to the formation of the semiconducting nature of the material. Fig. 7.12 shows the EDS spectra of 2.00 mol% ZrO_2 doped ZnO–

V_2O_5–Cr_2O_3 System (850CZ200) sintered at 850 °C at different regions, especially the grain interior and the grain boundary. EDS spectra of the ZnO grain boundary shows V, Cr and Zr segregation in the sample (850CZ200). Fig. 7.13 shows the EDS spectra of 2.00 mol% ZrO_2 doped ZnO–V_2O_5–Cr_2O_3 System (900CZ200) sintered at 900 °C at different regions, especially the grain interior and the grain boundary. EDS spectra of the ZnO grain boundary shows V, Cr and Zr segregation in the sample (900CZ200). Fig. 7.14 shows the EDS spectra of 2.00 mol% ZrO_2 doped ZnO–V_2O_5–Cr_2O_3 System (950CZ200) sintered at 950 °C at different regions, especially the grain interior and the grain boundary. EDS spectra of the ZnO grain boundary shows V, Cr and Zr segregation in the sample (950CZ200)

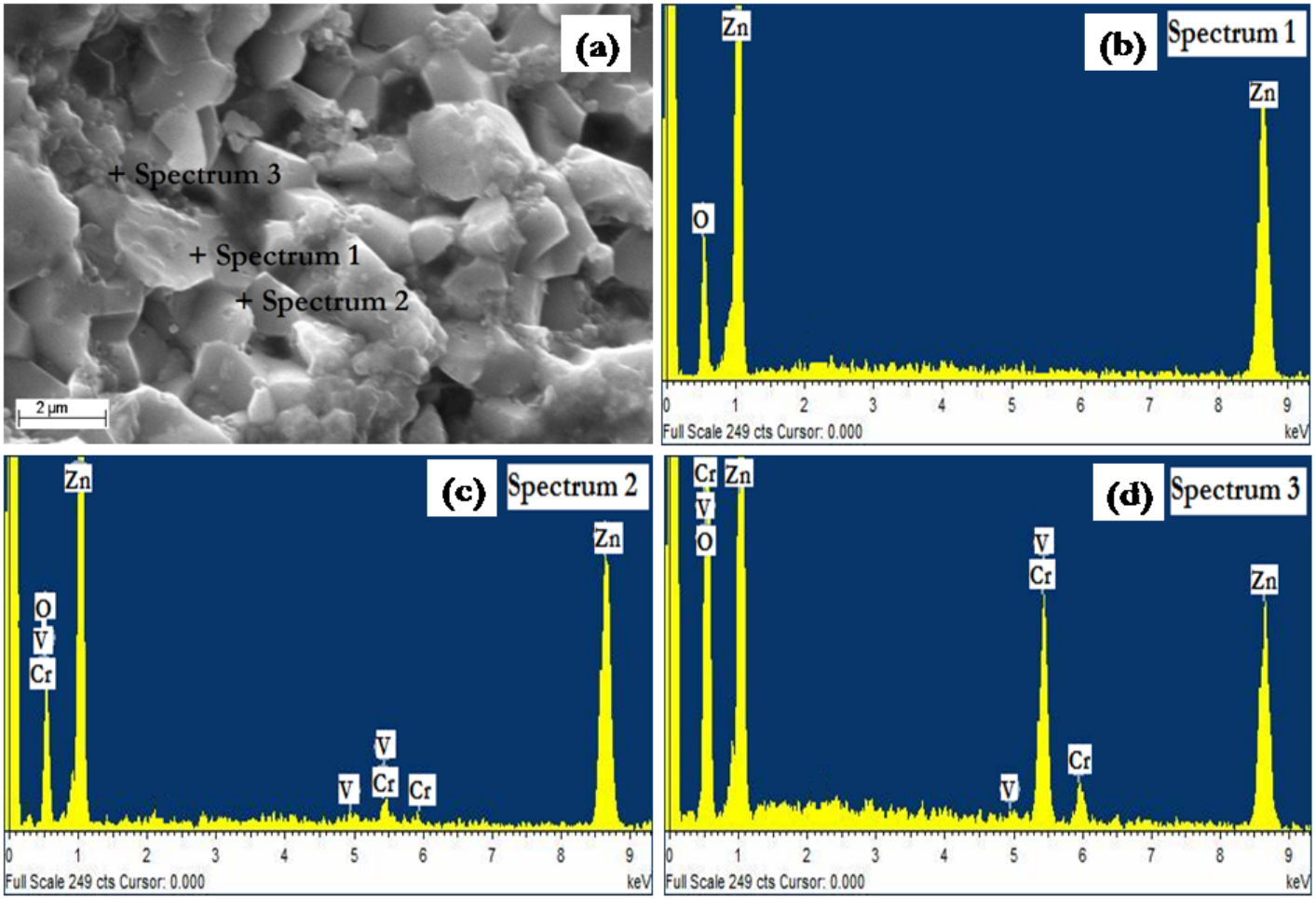

Figure 7.8: EDS spectra of 0.10 mol% ZrO_2 doped $ZnO–V_2O_5–Cr_2O_3$ System (900CZ010) sintered at 900 °C: (a) SEM micrograph (b) at the ZnO grain (c) at the ZnO grain boundary showing V and Cr segregation in it and (d) at the selected region.

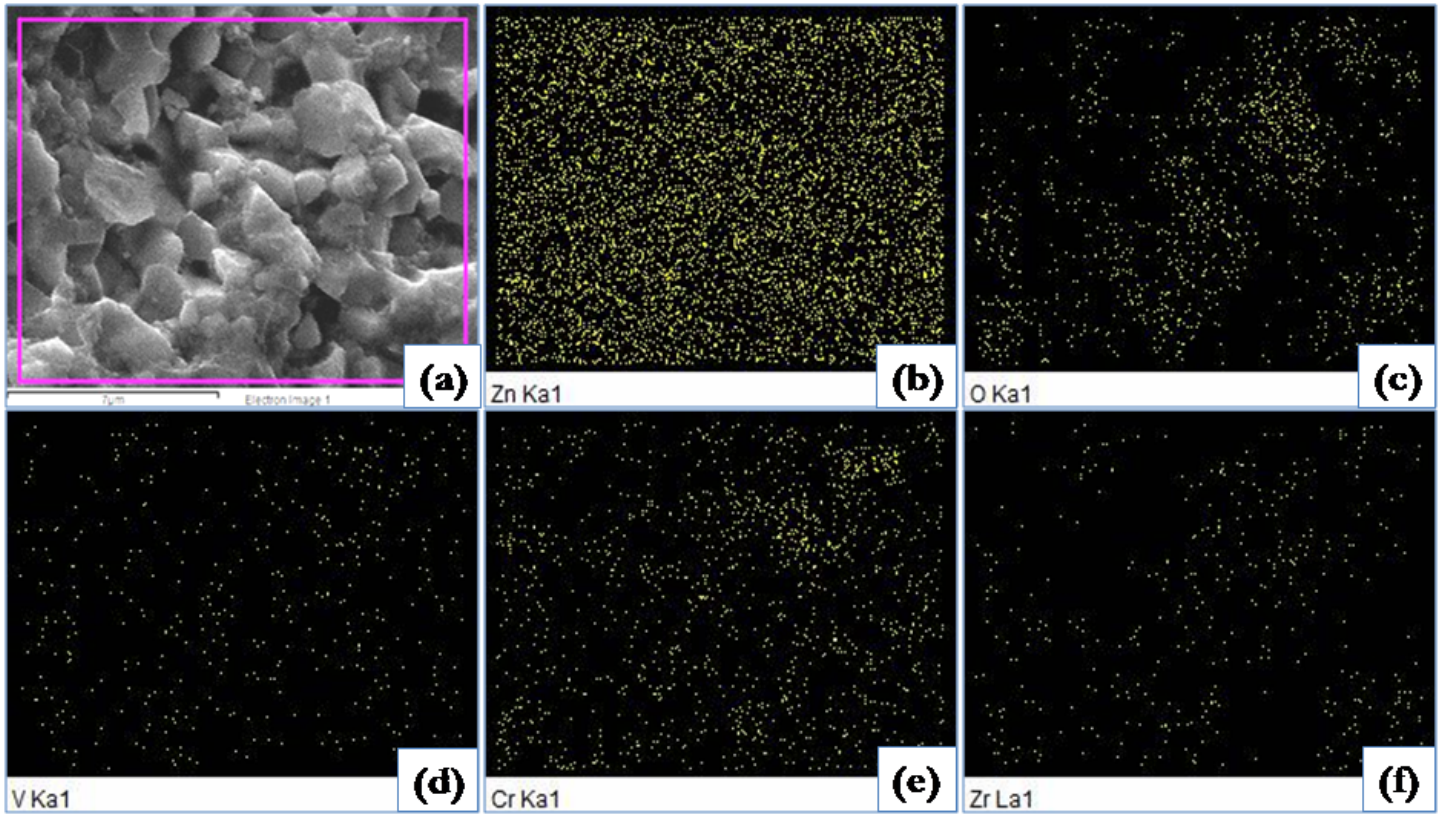

Figure 7.9: EDS elemental maps for 0.10 mol% ZrO_2 doped $ZnO–V_2O_5–Cr_2O_3$ System (900CZ010) sintered at 900 °C: (a) SEM micrograph (b) Zn map (c) O map (d) V map (e) Cr map and (f) Zr map

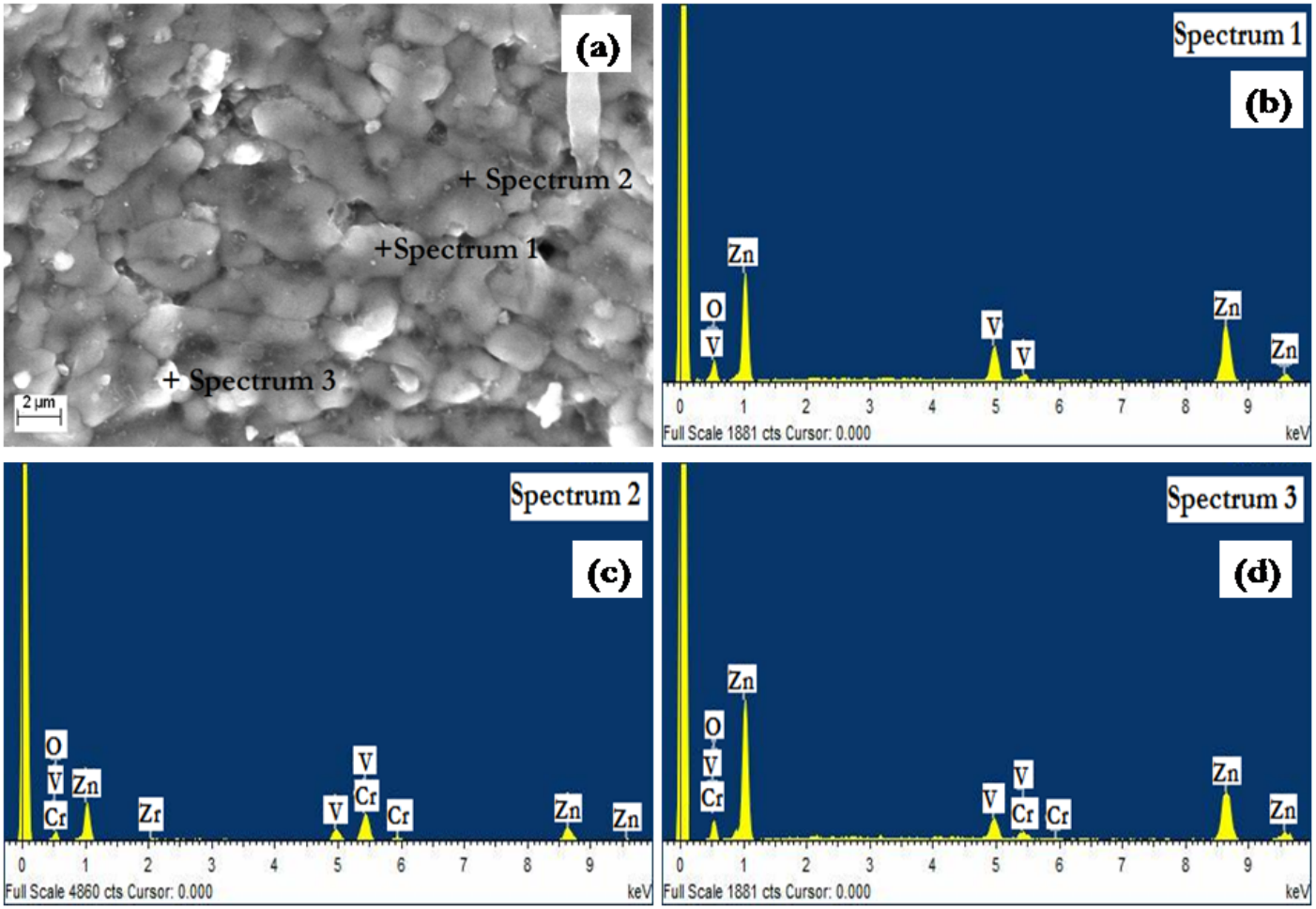

Figure 7.10: EDS spectra of 1.00 mol% ZrO_2 doped $ZnO–V_2O_5–Cr_2O_3$ System (900CZ100) sintered at 900 °C: (a) SEM micrograph (b) at the ZnO grain (c) at the ZnO grain boundary showing V, Cr and Zr segregation in it and (d) at the selected region.

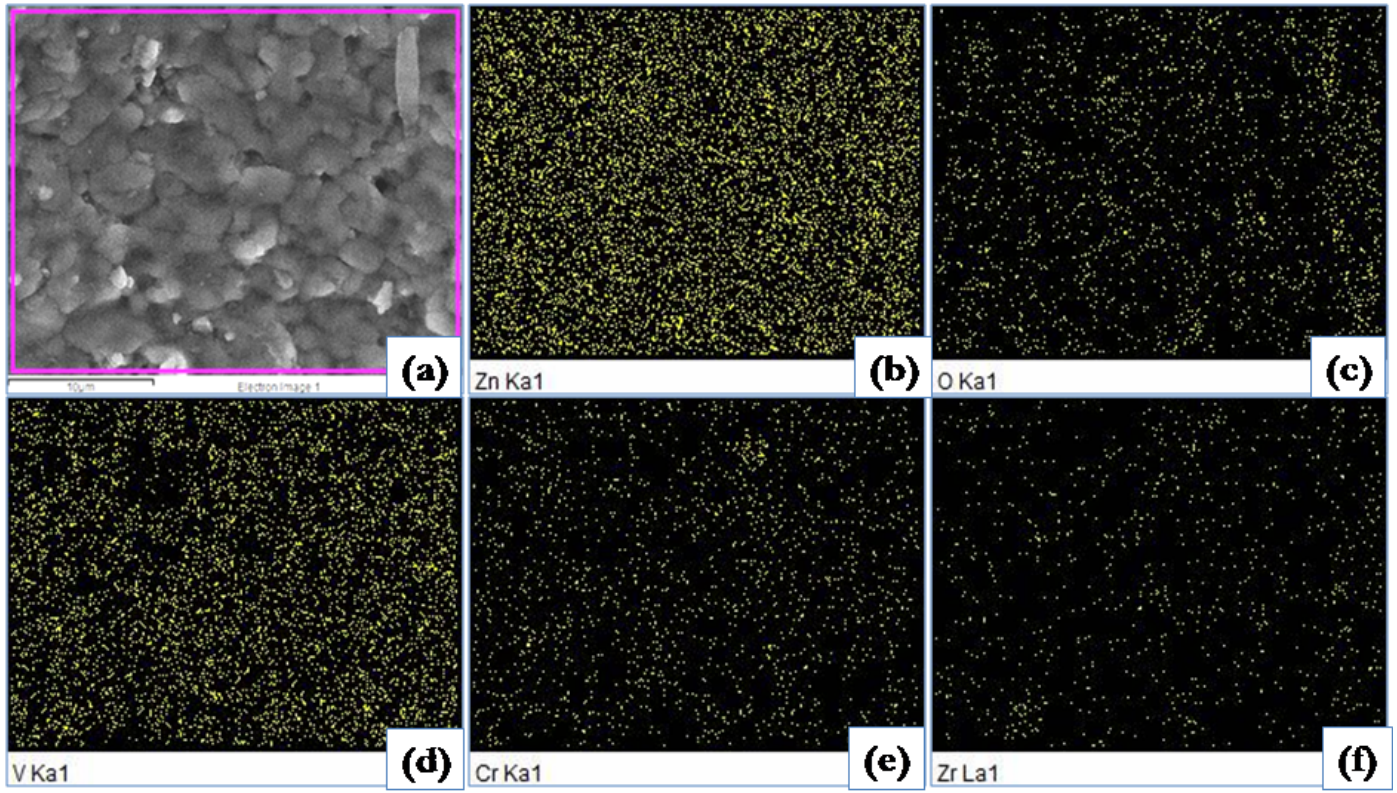

Figure 7.11: EDS elemental maps for 1.00 mol% ZrO_2 doped $ZnO–V_2O_5–Cr_2O_3$ System (900CZ100) sintered at 900 °C: (a) SEM micrograph (b) Zn map (c) O map (d) V map (e) Cr map and (f) Zr map.

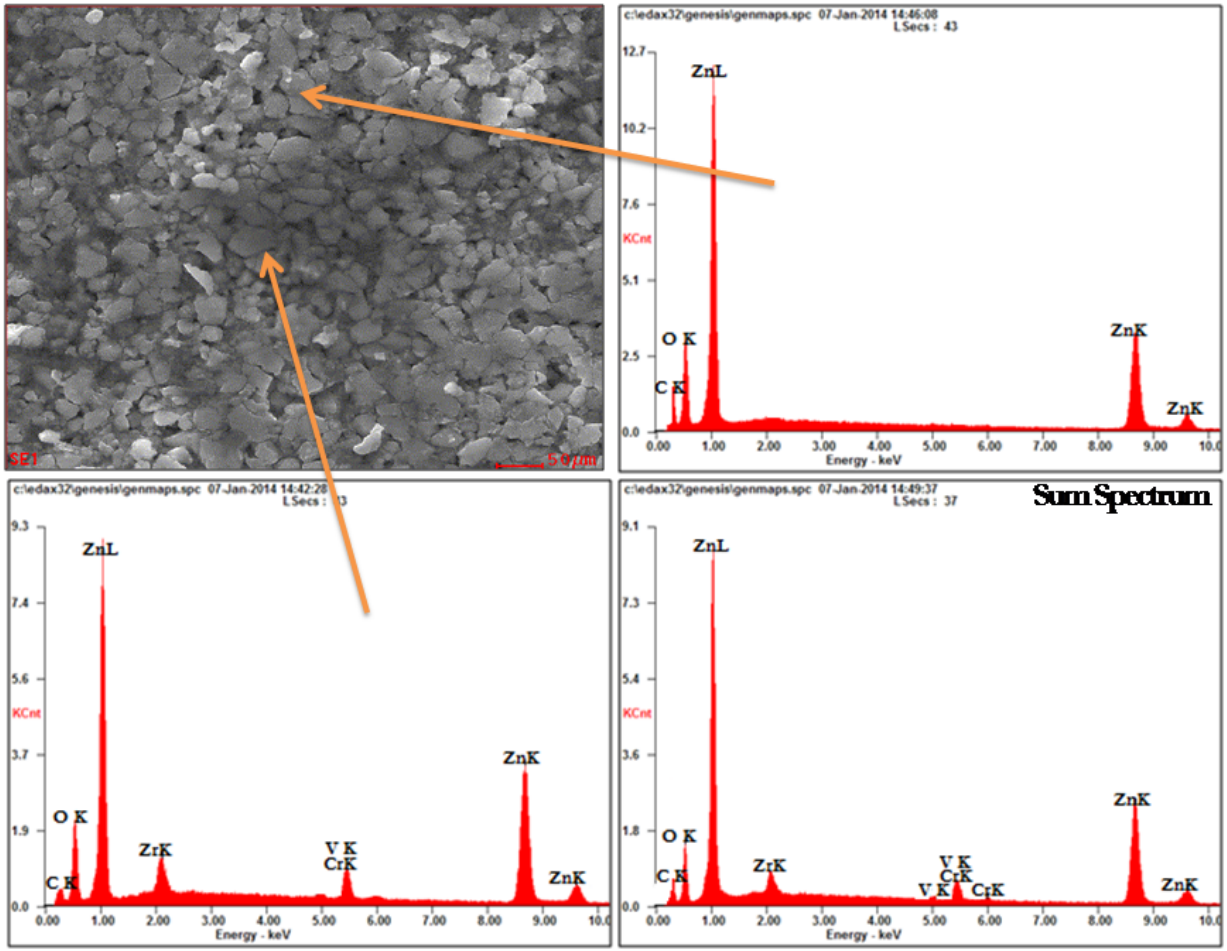

Figure 7.12: EDS spectra of 2.00 mol% ZrO_2 doped ZnO–V_2O_5–Cr_2O_3 System (850CZ200) sintered at 850 °C: (a) SEM micrograph (b) at the ZnO grain (c) at the ZnO grain boundary showing V, Cr and Zr segregation in it and (d) at the sum spectrum.

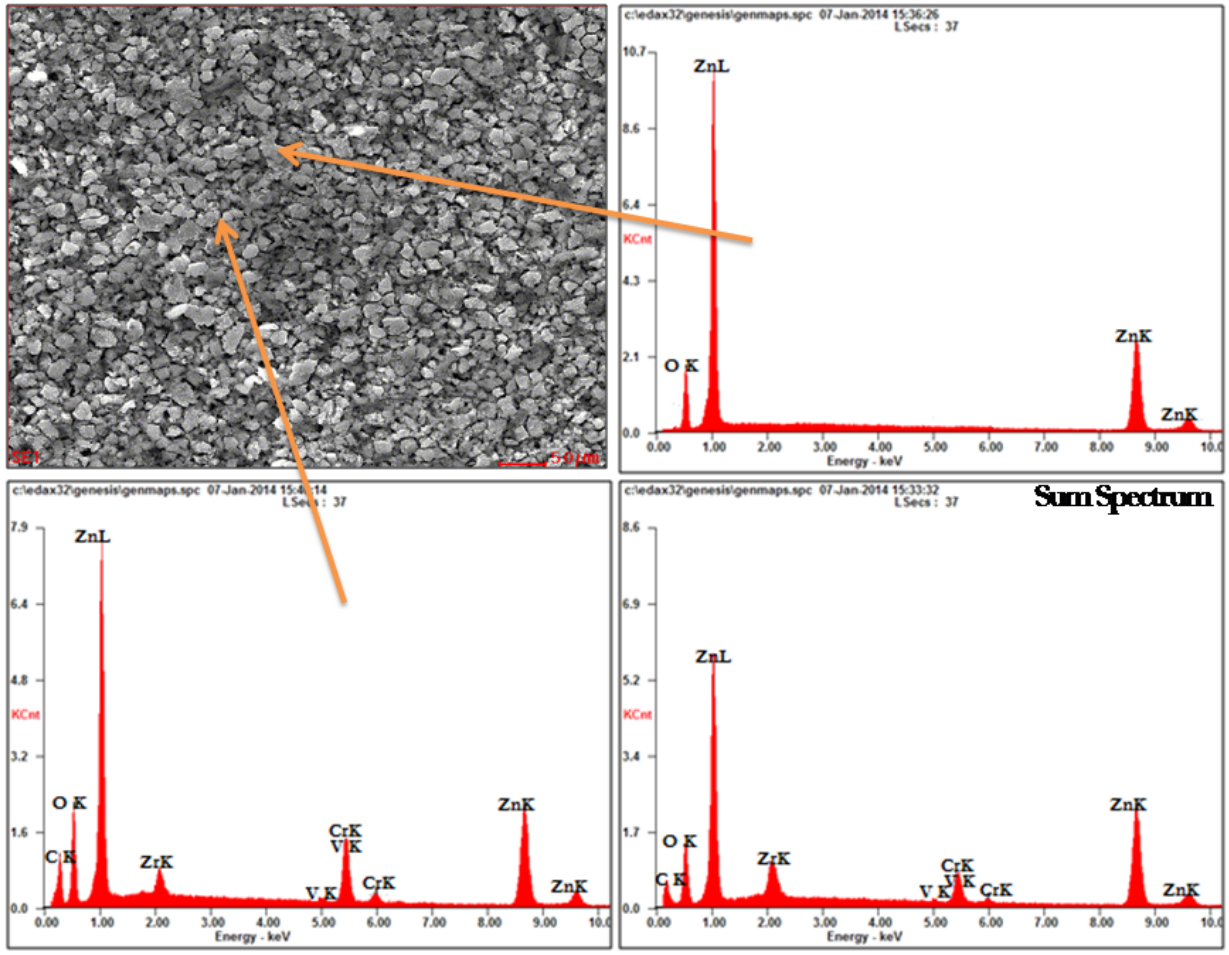

Figure 7.13: EDS spectra of 2.00 mol% ZrO_2 doped ZnO–V_2O_5–Cr_2O_3 System (900CZ200) sintered at 900 °C: (a) SEM micrograph (b) at the ZnO grain (c) at the ZnO grain boundary showing V, Cr and Zr segregation in it and (d) at the sum spectrum.

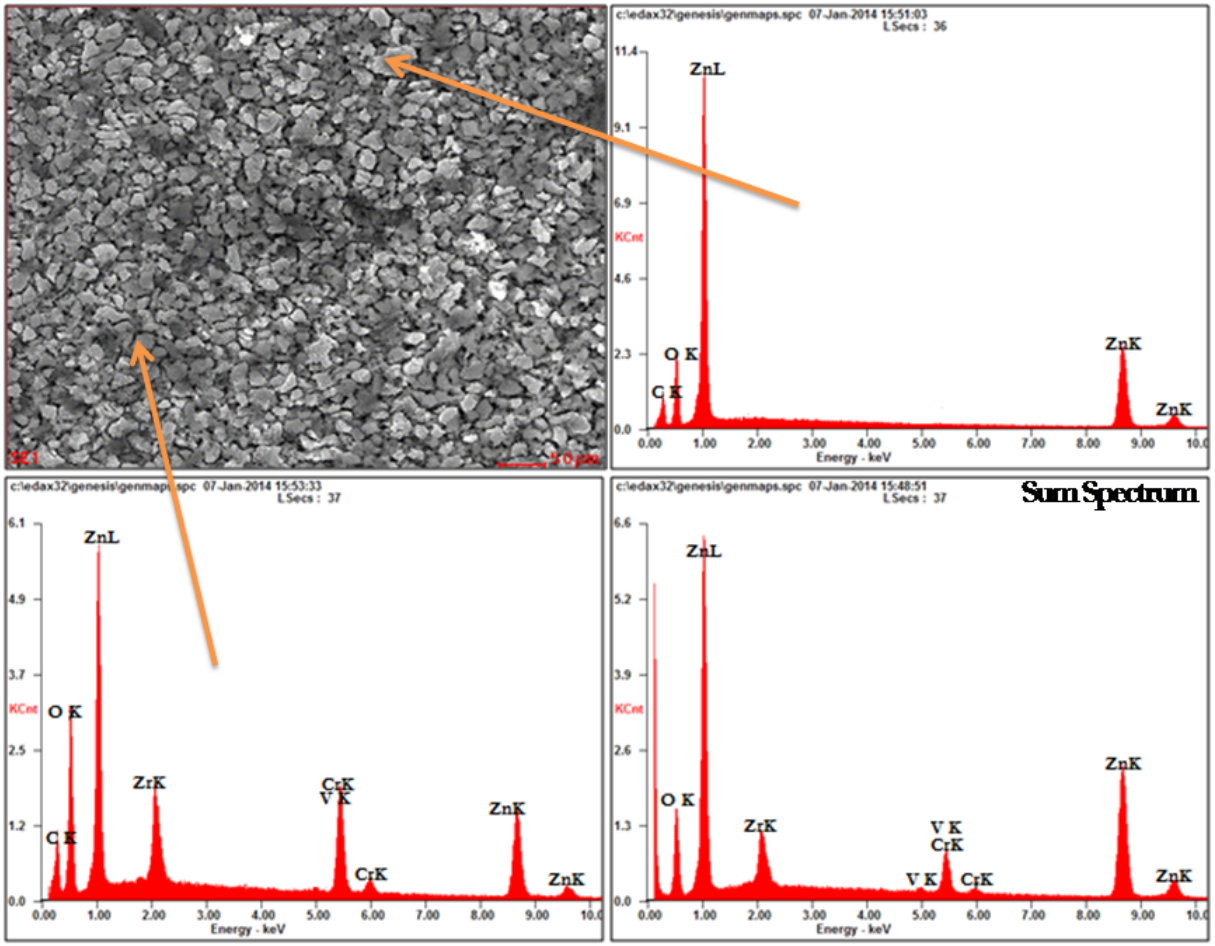

Figure 7.14: EDS spectra of 2.00 mol% ZrO_2 doped ZnO–V_2O_5–Cr_2O_3 System (950CZ200) sintered at 950 °C: (a) SEM micrograph (b) at the ZnO grain (c) at the ZnO grain boundary showing V, Cr and Zr segregation in it and (d) at the sum spectrum.

7.1.4. Percentage Theoretical Density.

Fig. 7.15(a) shows the plot between percentage theoretical density vs. mol% ZrO_2 for the samples sintered at 850˚C. The sintered density of the samples sintered at 850˚C was found to be in the range approximately 5.31-5.32 gm/cc (Table 7.1), corresponding to 93.37-93.89 % (Table 7.4) of the theoretical density (TD). The percentage theoretical density for 0.00, 0.10, 0.50, 1.00 and 2.00 mol% ZrO_2 doped $ZnO–V_2O_5–Cr_2O_3$ samples are 93.76, 93.72, 93.37, 93.84 and 93.89 % respectively.

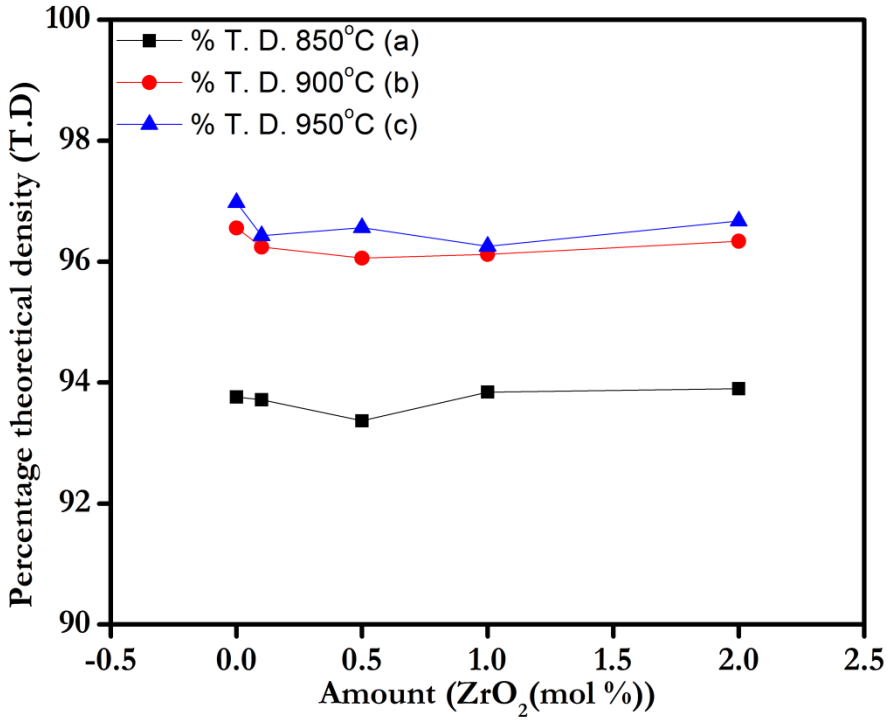

Fig.ure 7.15: shows the plot of percentage theoretical density vs. mol% ZrO_2 for the samples sintered at (a) 850 °C, (b) 900 °C & (c) 950 °C

Fig. 7.15(b) shows the plot between percentage theoretical density vs. mol% ZrO_2 for the samples sintered at 900˚C. The sintered density of the samples sintered at 900˚C were found to be approximately 5.46-5.48 gm/cc, corresponding to 96.12-96.55% of the theoretical density (TD) given in Table 7.5 and 7.2 respectively. The percentage theoretical density for 0.00, 0.10, 0.50, 1.00 and 2.00 mol% ZrO_2 doped $ZnO–V_2O_5–Cr_2O_3$ samples are 96.55, 96.24, 96.06, 96.12 and 96.34 % respectively

Fig. 7.15(c) shows the plot between percentage theoretical density vs. mol% ZrO_2 for the samples sintered at 950˚C. The sintered density of the samples sintered at 950˚C was found to be in the range approximately 5.47-5.49 gm/cc, corresponding to 96.33-96.98% of the theoretical density (TD) given in Table 7.6 and 7.3 respectively. The percentage theoretical density for 0.00, 0.10, 0.50, 1.00 and 2.00 mol% ZrO_2 doped ZnO–V_2O_5–Cr_2O_3 samples are 96.98, 96.33, 96.56, 96.25 and 96.67 respectively. It was assumed that the decrease of the sintered density is ascribed to the volatility of the V-species for V_2O_5 with a low melting point. The percentage theoretical density increases with increases in sintering temperature as well as ZrO_2 doping level.

7.2. Electrical Behavior of ZrO_2 Doped ZnO–V_2O_5–Cr_2O_3 Varistor.

7.2.1. Non-Linear properties

The varistor properties are featured by the conduction characteristics, which do not follow Ohm's law in the E–J relation. Basically, the curves are divided into two regions: one is a linear insulating region with high resistance before breakdown field and other is a nonlinear conducting region with low resistance after the breakdown field. The sharp knee of the curves leads to the better varistor properties.The behaviour of E_{1mA} in accordance with ZrO_2 content can be explained by the following expression:

$$E_{1mA} = V_{gb}/d, \qquad (7.1)$$

where d is the grain size, and V_{gb} is the breakdown voltage per grain boundary. This expression indicates that the V_{gb} value is directly determined from E_{1mA} [Levinson (1975)].

Fig. 7.16 shows the electric field–current density (E–J) characteristics of the samples sintered at 850 °C. The breakdown field (E_{1mA}) increased from 193 to 380 V/mm and then decreased to 319 V/mm with the further increase of the Zr content. Therefore, the decrease of E_{1mA} with the increase of the Zr content is attributed to the decrease of the breakdown voltage per grain boundary and the increase of the average ZnO grain size.

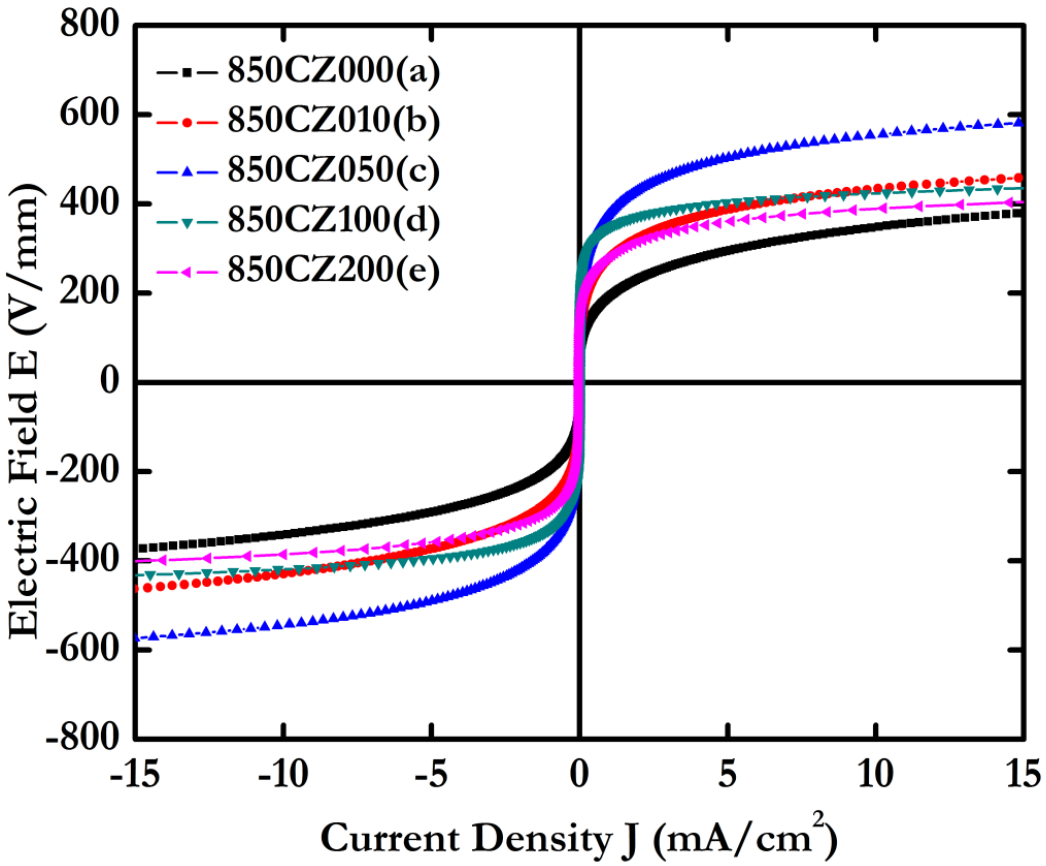

Figure 7.16: E-J curve showing the effects of ZrO_2 doped $ZnO–V_2O_5–Cr_2O_3$ samples sintered at 850°C: (a) 850CZ000 (0.00 mol% ZrO_2); (b) 850CZ010 (0.10 mol% ZrO_2); (c) 850CZ050 (0.50 mol% ZrO_2); (d) 850CZ100 (1.00 mol% ZrO_2) and (e) 850CZ200 (2.00 mol% ZrO_2)

Table 7.7: Summary of electrical results obtained for ZrO_2 doped $ZnO–V_2O_5–Cr_2O_3$ samples sintered at 850 °C

Sample Name	Non-ohmic coefficient α	Breakdown field E_{1mA} (V/mm)	Leakage current density J_L (μA/cm²)	Vgb (V/gb)	ε' (1KHz)	Tan δ (1KHz)
850CZ000	3.9	193	419.4	0.46	360	0.424
850CZ010	5.2	337	339.6	0.57	245	0.199
850CZ050	6.0	380	289.6	0.79	218	0.292
850CZ100	10.6	348	117.4	0.45	216	0.267
850CZ200	7.5	319	425.0	0.35	386	0.250

The leakage current density decreased from 419.4 to 117.4 μA/cm^2 with increasing content of Zr. However, further increase in the Zr content caused J_L to increase to 425.0 μA/cm^2, as shown in Fig. 7.16. The increase of J_L is attributed to the increase of the minority carriers in the grain boundary. The nonlinear coefficient (α) was increased from 3.9 to 10.6 with increasing content of Zr. However, further increase caused α to decrease upto 7.5, as shown in Fig. 7.16. As a result, it can be seen that the Zr content has a significant effect on the nonlinear properties of these ceramics in light of a variation. The E–J characteristic parameters are summarized in Table 7.7. The reduction in the number of grain boundaries per unit thickness due to grain enlargement should have caused of decrease in α value.

Fig. 7.17 shows the electric field–current density (E–J) characteristics of the samples sintered at 900 °C. The breakdown field (E_{1mA}) increased from 308 to 662 V/mm and then decreased to 563 V/mm with the increase of the Zr content. Therefore, the decrease of E_{1mA} with the increase of the Zr content is attributed to the decrease of the breakdown voltage per grain boundary and the increase of the average ZnO grain size. The leakage current density decreased from 128.3 to 120.1 μA/cm^2 with increasing content of Zr. However, further increase in the Zr content caused J_L to increase to 182.6 μA/cm^2, as shown in Fig. 7.17. The increase of J_L is attributed to the increase of the minority carriers in the grain boundary. The leakage current increases with the increase of ZrO_2 content. The reason is that electric ZrO_2 is filled in considerably between the ZnO grains. When applying voltage, part circuits form the pathway.

The nonlinear coefficient (α) was increased from 11.1 to 19.5 with increasing content of Zr. However, further increase caused α to decrease to 14.6, as shown in Fig. 7.17. As a result, it can be seen that the Zr content has a significant effect on the nonlinear properties of these ceramics in light of a variation. The E–J characteristic parameters are summarized in Table 7.8. The reduction in the number of grain boundaries per unit thickness due to grain enlargement should have caused of decrease in α value.

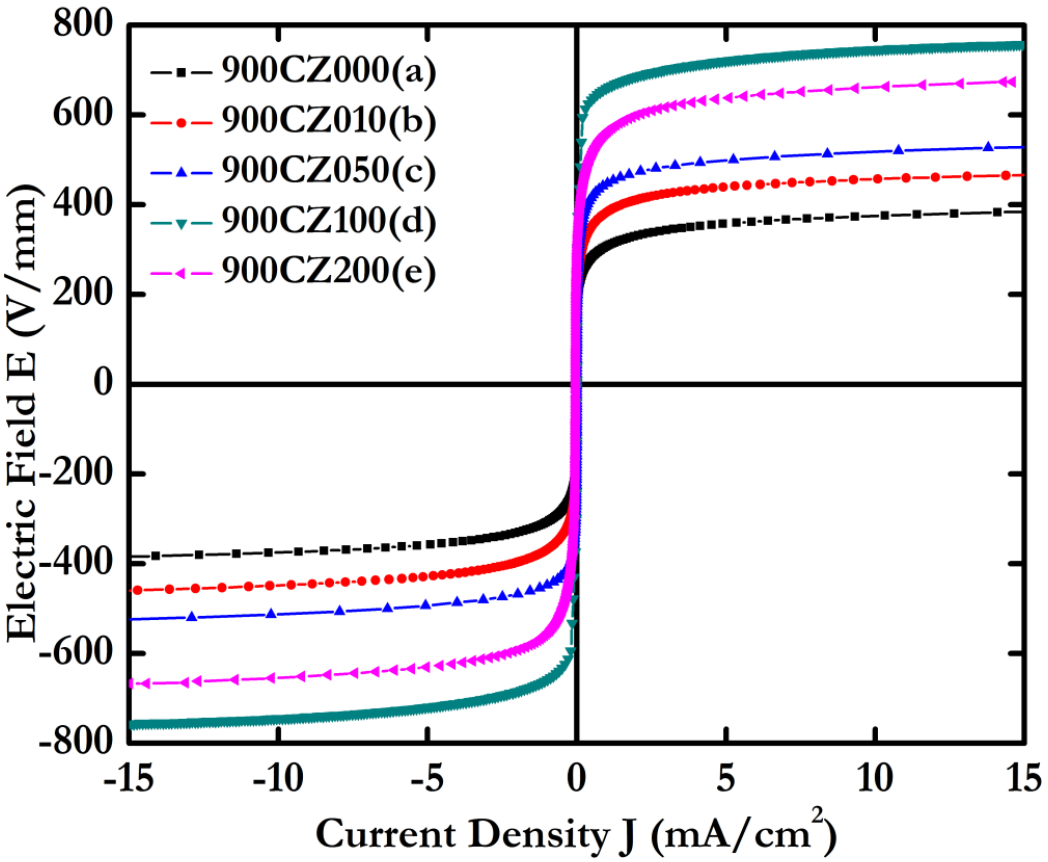

Figure 7.17: E-J curve showing the effects of ZrO_2 doped $ZnO–V_2O_5–Cr_2O_3$ samples sintered at 900 °C: (a) 900CZ000 (0.00 mol% ZrO_2); (b) 900CZ010 (0.10 mol% ZrO_2); (c) 900CZ050 (0.50 mol% ZrO_2); (d) 900CZ100 (1.00 mol% ZrO_2) and (e) 900CZ200 (2.00 mol% ZrO_2)

Table 7.8: Summary of electrical results obtained for ZrO_2 doped $ZnO–V_2O_5–Cr_2O_3$ samples sintered at 900 °C

Sample name	Non-ohmic coefficient α	Breakdown field E_{1mA} (V/mm)	Leakage current density J_L (μA/cm²)	Vgb (V/gb)	ε' (1KHz)	Tan δ (1KHz)
900CZ000	11.1	308	128.3	1.17	477	0.371
900CZ010	13.2	384	134.5	1.19	448	0.208
900CZ050	16.1	448	127.5	1.16	296	0.272
900CZ100	19.5	662	120.1	1.12	218	0.293
900CZ200	14.6	563	182.6	0.79	198	0.176

Fig. 7.18 shows the electric field–current density (E–J) characteristics of the samples sintered at 950 °C. The breakdown field (E_{1mA}) increased from 297 to 323 V/mm and then decreased to 208 V/mm with the increase of the Zr content. Therefore, the decrease of E_{1mA} with the increase of the Zr content is attributed to the decrease of the breakdown voltage per grain boundary and the increase of the average ZnO grain size. The leakage current density decreased from 429.1 to 117.2 μA/cm^2 with increasing content of Zr. However, further increasing Zr content caused J_L to increase to 335.0 μA/cm^2, as shown in Fig. 7.18. The increase of J_L is attributed to the increase of the minority carriers in the grain boundary.

The nonlinear coefficient (α) was increased from 4.0 to 15.2 with increasing content of Zr. However, further increase caused α to decrease upto 5.5, as shown in Fig. 7.18. As a result, it can be seen that the Zr content has a significant effect on the nonlinear properties of these ceramics in light of a variation. The E–J characteristic parameters are summarized in Table 7.9. The reduction in the number of grain boundaries per unit thickness due to grain enlargement should have caused a decrease in α value. This suggests that segregation of Zr in the grain boundary promoted the development of the essential potential barrier at the interface. Adversely, excessive Zr doping encouraged thicker grain bondary formation that could lead to poor non-linearity and lower bulk resistance. The behaviour of α in accordance with the Zr content can be related to the variation of the Schottky barrier height according to the variation of the electronic states at the grain boundaries.

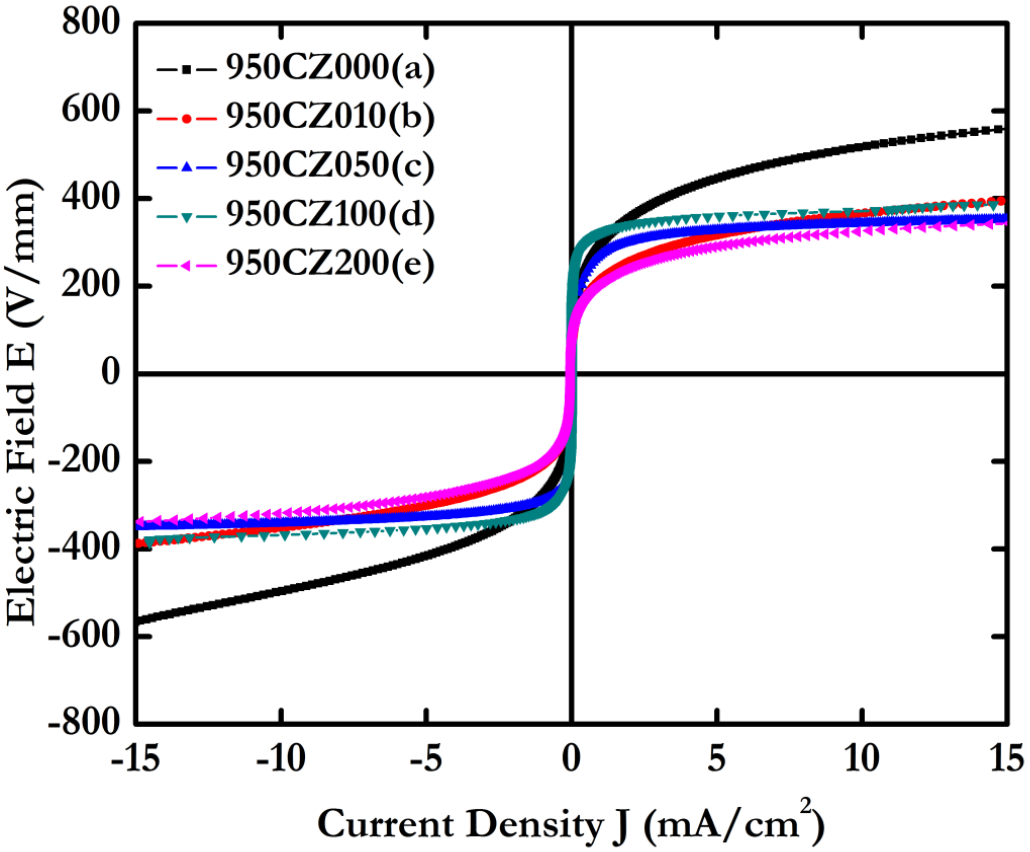

Figure 7.18: E-J curve showing the effects of ZrO_2 doped $ZnO–V_2O_5–Cr_2O_3$ samples sintered at 950°C: (a) 950CZ000 (0.00 mol% ZrO_2); (b) 950CZ010 (0.10 mol% ZrO_2); (c) 950CZ050 (0.50 mol% ZrO_2); (d) 950CZ100 (1.00 mol% ZrO_2) and (e) 950CZ200 (2.00 mol% ZrO_2)

Table 7.9: Summary of Electrical Results obtained for ZrO_2 doped $ZnO–V_2O_5–Cr_2O_3$ samples sintered at 950°C

Sample name	Non-ohmic coefficient α	Breakdown field E_{1mA} (V/mm)	Leakage current density J (μA/cm²)	Vgb (V/gb)	ε' (1KHz)	Tan δ (1KHz)
950CZ000	4.0	297	429.1	1.21	805	0.585
950CZ010	4.6	216	365.0	0.75	224	0.311
950CZ050	10.4	274	349.5	1.23	198	0.175
950CZ100	15.2	323	117.2	0.71	228	0.427
950CZ200	5.5	208	335.0	0.52	194	0.148

The non-linear property of the varistors is explained by the existence of potential barrier at the grain boundaries. In practice, there are a variety of inter-grain conduction paths that operate in parallel in varistors. They operate through the grain boundary region or through the bulk inter-granular material. In fact, transition metal oxides are involved in the formation of interfacial states and deep bulk traps at grain boundaries, providing large potential barriers to give better nonlinear characteristics. This barrier is schottky type in which, conduction in linear region is dominated by thermionic emission over this schottky barrier. Thus it is clear that vanadium ions play an important role in the non-linear conductivity of the prepared ceramics and it is important to discuss the defect chemistry induced by doping ZnO with V_2O_5.

7.2.2. Dielectric Spectroscopy

Fig. 7.19 shows the dielectric characteristics of the samples sintered at 850 °C with different amounts of ZrO_2.The ε' and tan δ at 1KHz for the 0.00, 0.10, 0.50, 1.00 and 2.00 mol% ZrO_2 doped $ZnO–V_2O_5–Cr_2O_3$ samples sintered at 850 °C are 360, 245, 218, 216, 386 and 0.424, 0.199, 0.292, 0.267, 0.250 respectively given in Table 7.7. At lower frequencies, a high relative dielectric permittivity was found. The dispersion of the dielectric properties is obvious. The formation of the grain boundary barrier layer was also confirmed by the rapid decrease of the apparent dielectric constant with increasing frequency of the ceramics and the non-ohmic I-V behaviour.

Fig. 7.20 shows the dielectric characteristics of the samples sintered at 900 °C with different amounts of ZrO_2.The ε' and tan δ at 1KHz for the 0.00, 0.10, 0.50, 1.00 and 2.00 mol% ZrO_2 doped $ZnO–V_2O_5–Cr_2O_3$ samples sintered at 900 °C are 477, 448, 296, 218, 198 and 0.371, 0.208, 0.272, 0.293, 0.176 respectively given in Table 7.8. Heterogeneities in the grains and/or the presence of the potential barriers between the grains are responsible for the similar dielectric properties in a number of materials. Orientational polarization (zinc interstitials and oxygen vacancies) is dominant at higher frequencies, whereas the high degree of dispersion observed at the low-frequency region is attributable to interfacial polarization.

Fig. 7.21 shows the dielectric characteristics of the samples sintered at 950 °C with different amounts of ZrO_2. The ε' and tan δ at 1KHz for the 0.00, 0.10, 0.50, 1.00 and 2.00 mol% ZrO_2 doped $ZnO–V_2O_5–Cr_2O_3$ samples sintered at 950 °C are 805, 224, 198, 228, 194 and 0.585, 0.311, 0.175, 0.427, 0.148 respectively given in Table 7.9. As the amount of ZrO_2 increased, the dielectric constant (έ) decreased with less sharp dispersive drop with increasing frequency, which is closely associated with the polarization of dielectrics. It is assumed that this is attributed to the decrease of the number of dipole, which can follow the test frequency.

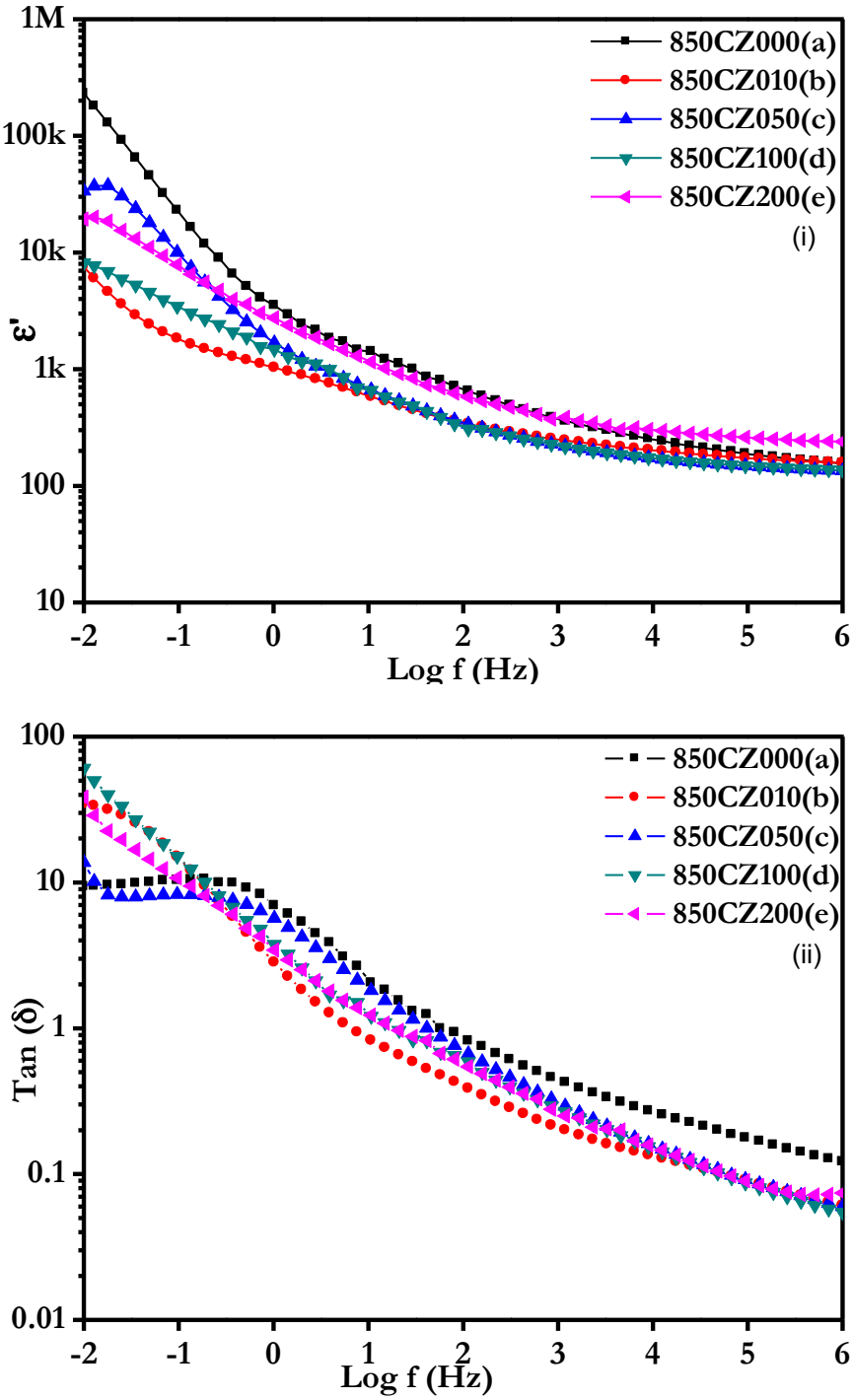

Figure 7.19: Dielectric spectroscopy (i) ε'& (ii) Tan δ, showing the effects of ZrO_2 doped $ZnO–V_2O_5–Cr_2O_3$ samples sintered at 850 °C: (a) 850CZ000 (0.00 mol% ZrO_2); (b) 850CZ010 (0.10 mol% ZrO_2); (c) 850CZ050 (0.50 mol% ZrO_2); (d) 850CZ100 (1.00 mol% ZrO_2) and (e) 850CZ200 (2.00 mol% ZrO_2)

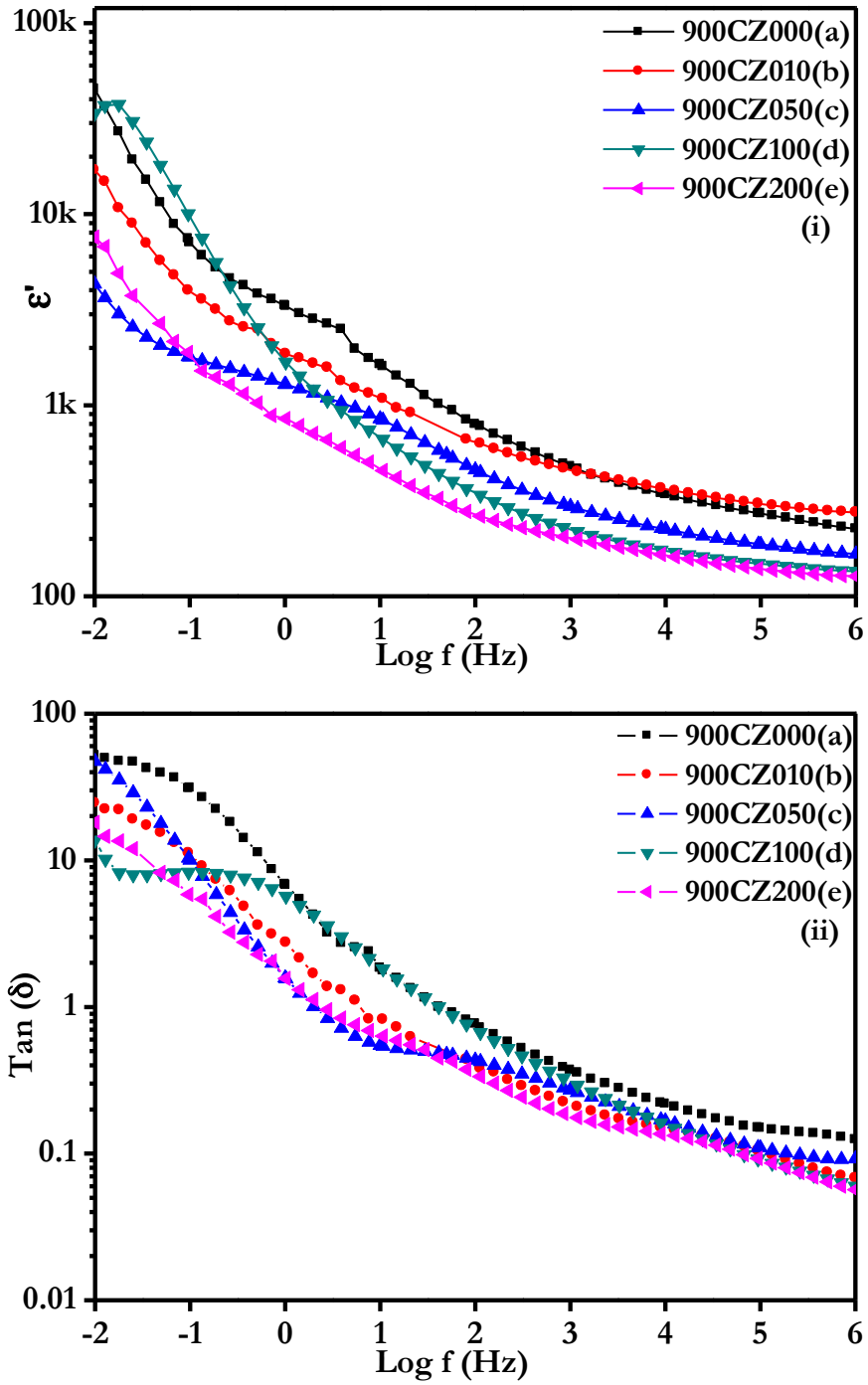

Figure 7.20: Dielectric spectroscopy (i) ε' & (ii) Tan δ, showing the effects of ZrO_2 doped $ZnO–V_2O_5–Cr_2O_3$ samples sintered at 850 °C: (a) 900CZ000 (0.00 mol% ZrO_2); (b) 900CZ010 (0.10 mol% ZrO_2); (c) 900CZ050 (0.50 mol% ZrO_2); (d) 900CZ100 (1.00 mol% ZrO_2) and (e) 900CZ200 (2.00 mol% ZrO_2)

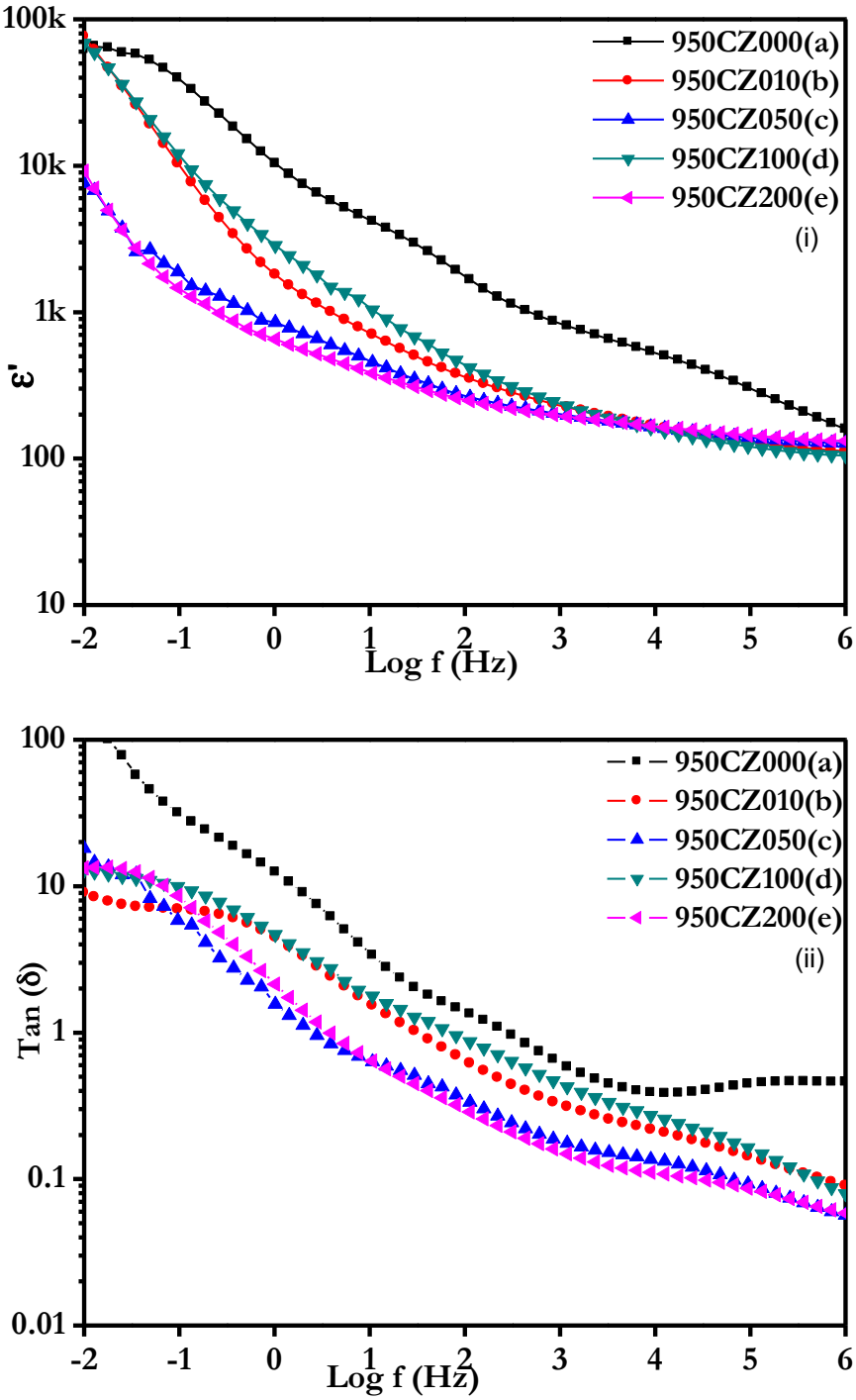

Figure 7.21: Dielectric spectroscopy (i) ε' & (ii) Tan δ, showing the effects of ZrO_2 doped $ZnO–V_2O_5–Cr_2O_3$ samples sintered at 950 °C: (a) 950CZ000 (0.00 mol% ZrO_2); (b) 950CZ010 (0.10 mol% ZrO_2); (c) 950CZ050 (0.50 mol% ZrO_2); (d) 950CZ100 (1.00 mol% ZrO_2) and (e) 950CZ200 (2.00 mol% ZrO_2)

It is observed that the ε' measuring within the frequency depends on the amount of ZrO_2. This is directly related to the average grain size and depletion layer width, as can be seen in the following expression:

$$\varepsilon' = \mathcal{E}_g \frac{d}{t} \tag{7.2}$$

where έ is the dielectric constant of ZnO (8.5), d is the average grain size, and t is the depletion layer width of the both sides at the grain boundaries. The decrease of d/t ratio in $\varepsilon' = \mathcal{E}_g \frac{d}{t}$ gives rise to the decrease of the ε'. For the samples sintered at 900°C, the έ at 1 kHz decreased from 477 to 198. The detailed dielectric parameters are summarized in Tables from 7.7 to 7.9.

7.2.3. Impedance Spectroscopy

The semicircle curves observed in Figs. 7.22 to 7.30 (a-e). It was analysed by convolution of two time constant in the system. Thus, the equivalent circuit containing two parallel resistance-constant phase element (CPE) sub-circuits in series was used for fitting the impedance spectra which is shown from Figs. 7.22 to 7.30 (f). Use of a simple capacitor is not adequate to model the electrical response of the material due to the microstructural heterogeneities of the sample. The appearance of full and partial semicircles or no semicircle depends upon the strength of relaxation and the available frequency range [Bueno et al. (1998); Pattanayak et al. (2014); Choudhary et al. (2013); West et al. (1997)], although these semicircles are depressed. This behaviour manifests that there is a distribution of relaxation times instead of a single relaxation time in the material and confirms the presence of a non-debye type relaxation in the materials. In most real cases related to ceramic materials, the Nyquist plot is depressed, with its centre below the real axis. A perfect semicircle with its centre on the Z'-axis is observed for ideal debye-type relaxation. However, in the studied material, we did not find such debye-type relaxation [Tsai et al. (1994); (1996)]. A constant phase element (CPE) is used to represent the non-ideal debye type behaviour, which has impedance given by Abram et al. [2003], and is introduced with the resistors and capacitors or a CPE. The CPE is equivalent to a

distribution of capacitors in parallel. The impedance function of the CPE element is

$$Z_{CPE} = \frac{1}{P(j\omega)^n} \quad (7.3)$$

where P is a constant that is independent of frequency, ω = 2πf is the angular frequency (f is the applied frequency in Hz), $j = \sqrt{-1}$ and n is an exponential index, which is measure of arc depression. When constant n = 0, the CPE acts as a pure resistor with value = $1/P$, while n = 1 for ideal debye-like behaviour, in which, the CPE represents an ideal capacitor (C = P). The capacitor is frequency dependent when the n value is below unity. In most real cases of ceramic materials, the arc in complex impedance plots of Im (Z') versus Re (Z") is depressed, with its centre below the real axis. However, in polycrystalline semiconductor ceramics, the trapping of the charge at grain boundaries appears to have a significant effect on the electrical transport properties due to the formation of electrostatic potential barriers [Abram (2003)].

The electrode contribution to the overall electrolyte resistance has not been considered. A total of three regions were apparent. One region appears to be the highly conducting grain cores and was not considered further [West et al. (1997)].The other two regions represent the grain boundary regions that further split into low and high frequency regions; these regions were considered further in this work. Two hypotheses may be considered to explain these two time constants. The first hypothesis suggests that one time constant is related to the grain barrier and the second is associated with the grain boundary barrier. The limitation of this model is that the grain resistivity calculated at 50°C, 150°C & 250°C is higher than the literature values reported for grain resistivity of ZnO [West et al. (1997)]. The second hypothesis of the existence of different defects and/or adsorbed species at the grain boundary region, not necessarily at the same grain boundary. The two time constants may be the result of these types of defects. The second hypothesis is more feasible because the possibility of existence of different adsorbed species and defects on ZnO was observed in the literature [Bueno et al. (1998)].

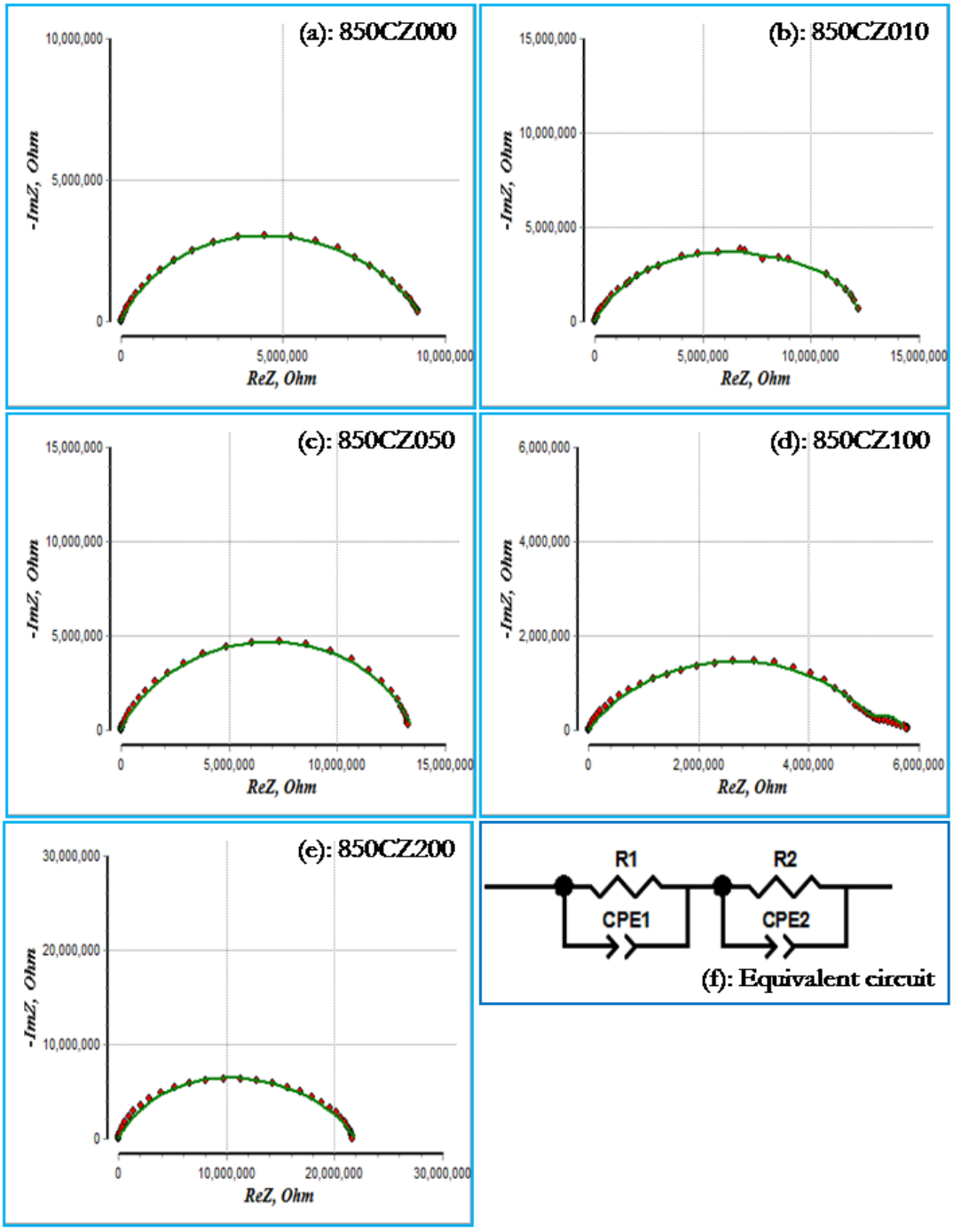

Figure 7.22: Experimental plots, fitted plots and equivalent circuit for fitting of impedance spectra of the samples as a function of ZrO_2 amount measured at 50 °C : (a) 850CZ000 (0.00 mol% ZrO_2); (b) 850CZ010 (0.10 mol% ZrO_2); (c) 850CZ050 (0.50 mol% ZrO_2); (d) 850CZ100 (1.00 mol% ZrO_2), (e) 850CZ200 (2.00 mol% ZrO_2) and (f) equivalent circuit.

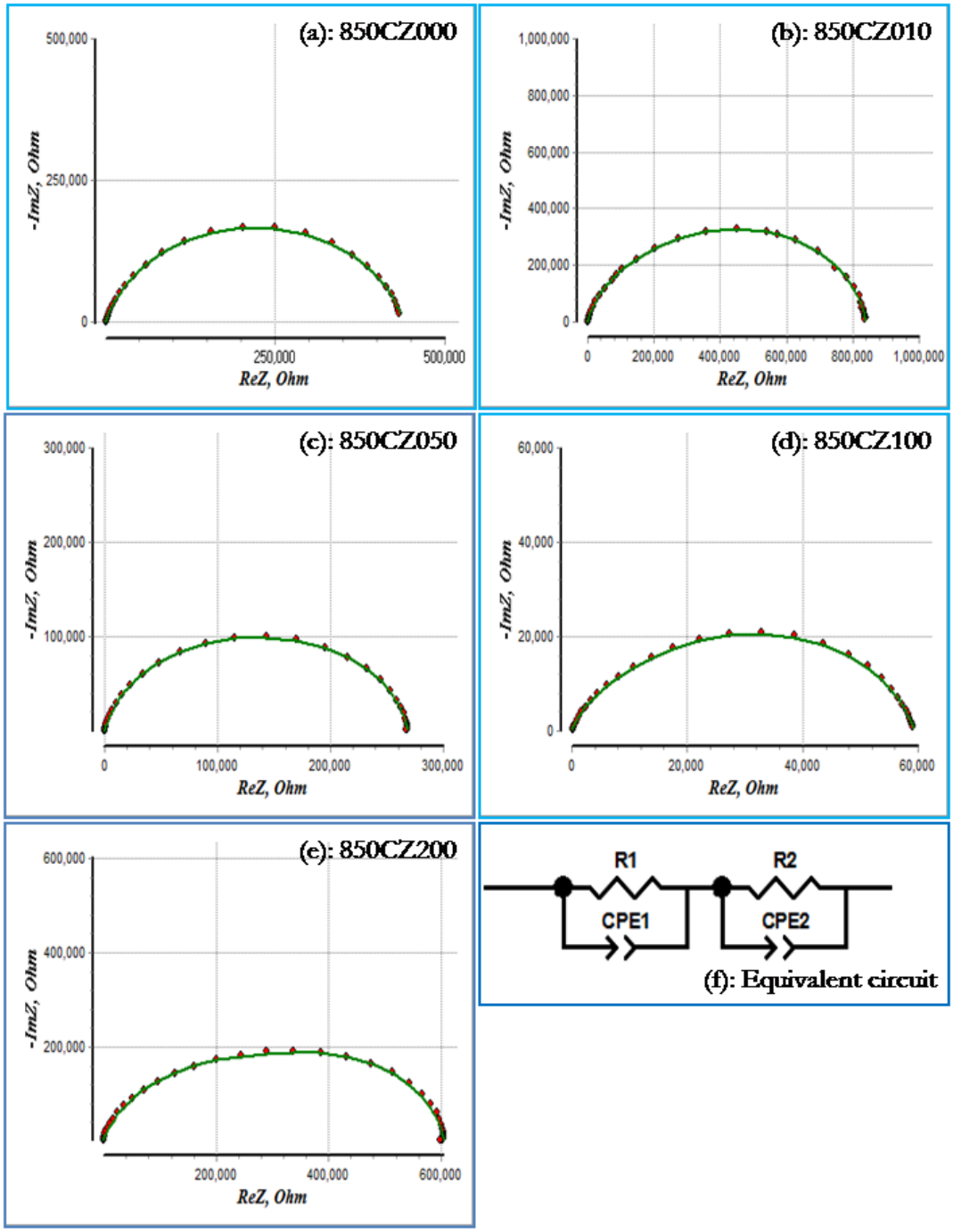

Figure 7.23: Experimental plots, fitted plots and equivalent circuit for fitting of impedance spectra of the samples as a function of ZrO_2 amount measured at 150 °C : (a) 850CZ000 (0.00 mol% ZrO_2); (b) 850CZ010 (0.10 mol% ZrO_2); (c) 850CZ050 (0.50 mol% ZrO_2); (d) 850CZ100 (1.00 mol% ZrO_2), (e) 850CZ200 (2.00 mol% ZrO_2) and (f) equivalent circuit.

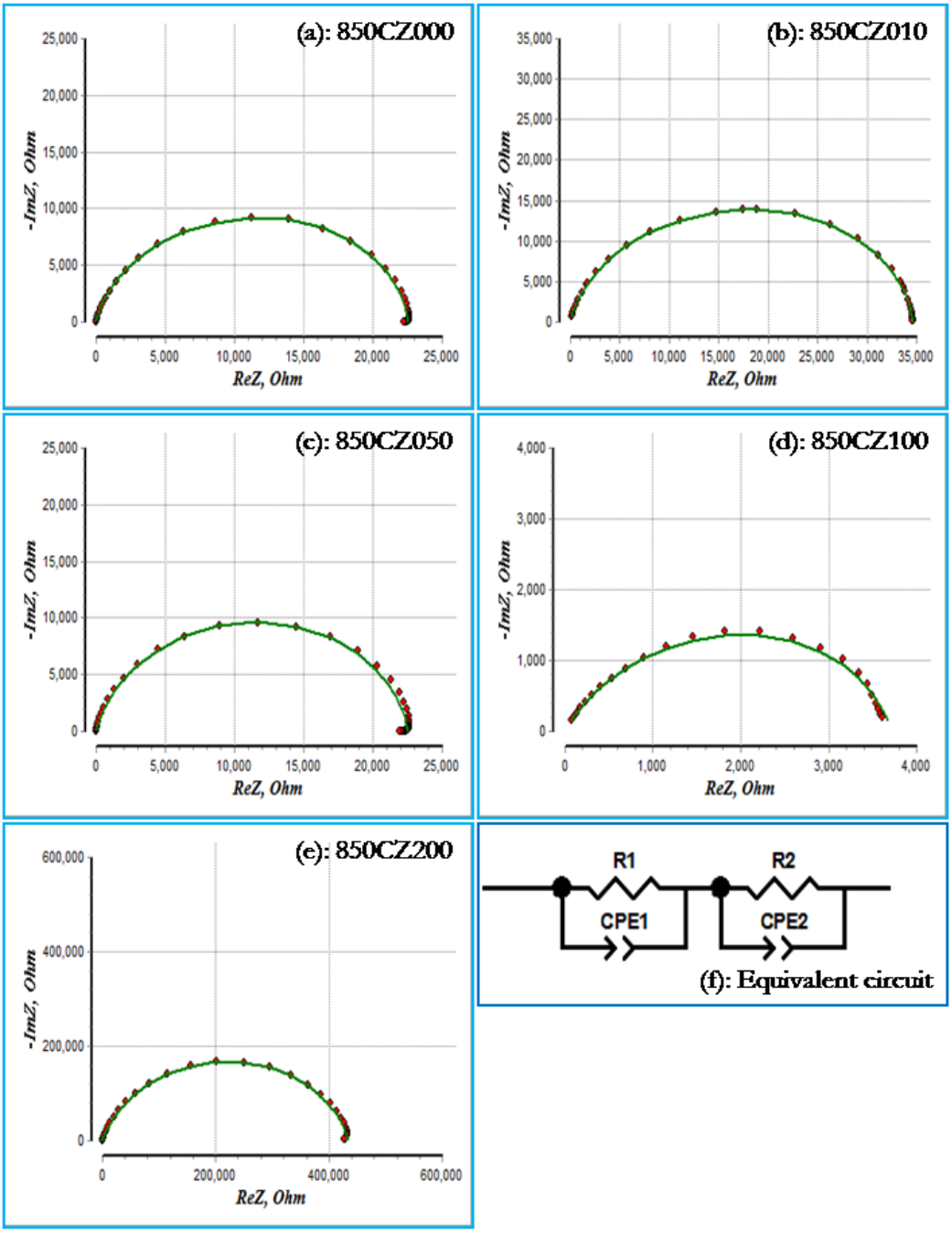

Figure 7.24: Experimental plots, fitted plots and equivalent circuit for fitting of impedance spectra of the samples as a function of ZrO_2 amount measured at 250 °C : (a) 850CZ000 (0.00 mol% ZrO_2); (b) 850CZ010 (0.10 mol% ZrO_2); (c) 850CZ050 (0.50 mol% ZrO_2); (d) 850CZ100 (1.00 mol% ZrO_2), (e) 850CZ200 (2.00 mol% ZrO_2) and (f) equivalent circuit.

To understand the influence of the microstructure and the potential barrier on the electrical properties of ZnO ceramics, the impedance spectra of ZnO pellets were fitted with the electrical equivalent circuit (Figs. 7.22 to 7.30 (f)). The proposed electrical model consists of parallel distributed capacitance represented by resistance R and P (constant phase element).

The results of the numerical equivalent circuit parameters fitting of plots using commercially available electrochemical impedance spectroscopy (EIS) [Bondarenko et al. (2005)] for all investigated structures are given in Table 7.10-7.18.

The order of magnitude of the 'P' suggests that the semicircle is due to grain boundaries, typically of a double-layer effect [Jonscher (1977); Jorcin et al. (2006)]. In Figs. 7.22 to 7.30 (f), R_1 and P_1 denote the resistance, and capacitance/CPE is assigned to the high-frequency defects and/or adsorbed species at the grain boundary region, not necessarily at the same grain boundary; R_2 and P_2 represent the resistance and capacitance/CPE of the low-frequency grain boundary of most resistive elements that dominate the impedance results. The two R-values obtained at 50 °C, 150 °C & 250 °C are given from Tables 7.10 to 7.18 and were obtained by plot fitting. These values were further used to evaluate the apparent activation energy for charge transport through the grain boundary.

Figs. 7.22, 7.23, 7.24 and Tables 7.10, 7.11, 7.12 shows the total resistance given by R_T (Ω) = R_1 (Ω) + R_2 (Ω) of the samples sintered at 850 °C with different amounts of ZrO_2 measured at 50 °C, 150 °C & 250 °C respectively. The R_T (Ω) for the the 0.00, 0.10, 0.50, 1.00 and 2.00 mol% ZrO_2 doped ZnO–V_2O_5–Cr_2O_3 samples measured at 50 °C are 8.27 x10^6, 1.23 x10^7, 1.25 x10^7, 5.72 x10^6, 2.09 x10^7; at 150 °C are 4.24 x10^5, 8.42 x10^5, 2.60 x10^5, 5.96 x10^4, 5.96 x10^5 and at 250 °C are 2.25 x10^4, 3.46 x10^4, 2.22 x10^4, 3.62 x10^3, 4.79 x10^4 (Ω) respectively. The total resistance R_T (Ω) measured at 50 °C for the sample doped with 2.00 mol% ZrO_2 is the maximum because of the small grain size; i.e., there are large number of grain boundaries.

Table 7.10: Summary of fitted electrical parameter obtained from EIS software for ZrO_2 doped samples sintered at 850 °C and measured at 50 °C.

Samples (at 50°C)	$R_1(\Omega)$	P_1	n_1	$R_2(\Omega)$	P_2	n_2	$R_T(\Omega)$
850CZ000	2.54×10^5	4.39×10^{-10}	1.00	8.02×10^6	9.77×10^{-10}	0.98	8.27×10^6
850CZ010	2.19×10^6	2.17×10^{-9}	0.85	1.01×10^7	4.21×10^{-9}	0.78	1.23×10^7
850CZ050	7.44×10^5	8.19×10^{-10}	1.00	1.18×10^7	1.82×10^{-9}	0.98	1.25×10^7
850CZ100	9.45×10^5	1.66×10^{-7}	0.96	4.78×10^6	2.30×10^{-8}	0.64	5.72×10^6
850CZ200	3.41×10^6	1.19×10^{-10}	0.95	1.75×10^7	5.09×10^{-10}	1.00	2.09×10^7

Table 7.11: Summary of fitted electrical parameter obtained from EIS software for ZrO_2 doped samples sintered at 850 °C and measured at 150 °C.

Samples (at 150°C)	$R_1(\Omega)$	P_1	n_1	$R_2(\Omega)$	P_2	n_2	$R_T(\Omega)$
850CZ000	1.86×10^4	1.06×10^{-9}	0.98	4.06E+05	1.24×10^{-9}	0.93	4.24×10^5
850CZ010	1.07×10^5	2.14×10^{-9}	0.89	7.35E+05	1.47×10^{-9}	0.90	8.42×10^5
850CZ050	3.73×10^4	1.04×10^{-9}	1.00	2.23E+05	1.74×10^{-9}	0.99	2.60×10^5
850CZ100	1.93×10^4	1.54×10^{-8}	0.81	4.03E+04	1.32×10^{-8}	0.83	5.96×10^4
850CZ200	1.27×10^5	1.2×10^{-10}	0.97	4.69E+05	6.9×10^{-10}	0.91	5.96×10^5

Table 7.12: Summary of fitted electrical parameter obtained from EIS software for ZrO_2 doped samples sintered at 850 °C and measured at 250 °C.

Samples (at 250°C)	$R_1(\Omega)$	P_1	n_1	$R_2(\Omega)$	P_2	n_2	$R_T(\Omega)$
850CZ000	1.85×10^3	1.15×10^{-9}	1.00	2.07×10^4	1.54×10^{-9}	0.93	2.25×10^4
850CZ010	6.56×10^3	3.26×10^{-9}	0.89	2.81×10^4	1.87×10^{-9}	0.91	3.46×10^4
850CZ050	3.74×10^3	1.20×10^{-9}	1.00	1.85×10^4	3.15×10^{-9}	1.00	2.22×10^4
850CZ100	1.04×10^3	3.86×10^{-8}	0.78	2.58×10^3	1.02×10^{-8}	0.94	3.62×10^3
850CZ200	1.35×10^4	1.24×10^{-10}	1.00	3.44×10^4	6.94×10^{-10}	0.90	4.79×10^4

Figs. 7.25, 7.26, 7.27 and Tables 7.13, 7.14, 7.15 shows the total resistance given by R_T (Ω) = R_1 (Ω) + R_2 (Ω) of the samples sintered at 900 °C with different amounts of ZrO_2 measured and calculated at 50 °C, 150 °C & 250 °C. The R_T (Ω) for the the 0.00, 0.10, 0.50, 1.00 and 2.00 mol% ZrO_2 doped $ZnO–V_2O_5–Cr_2O_3$ samples measured at 50 °C are 6.26×10^7, 1.32×10^7, 7.68×10^7, 1.20×10^8, 1.17×10^8; at 150 °C are 5.31×10^5, 3.38×10^5, 6.99×10^5,1.39×10^6, 8.24×10^5 and at 250 °C are 1.26×10^4, 2.30×10^4, 1.65×10^4, 2.87×10^4, 3.14×10^4 Ω respectively.

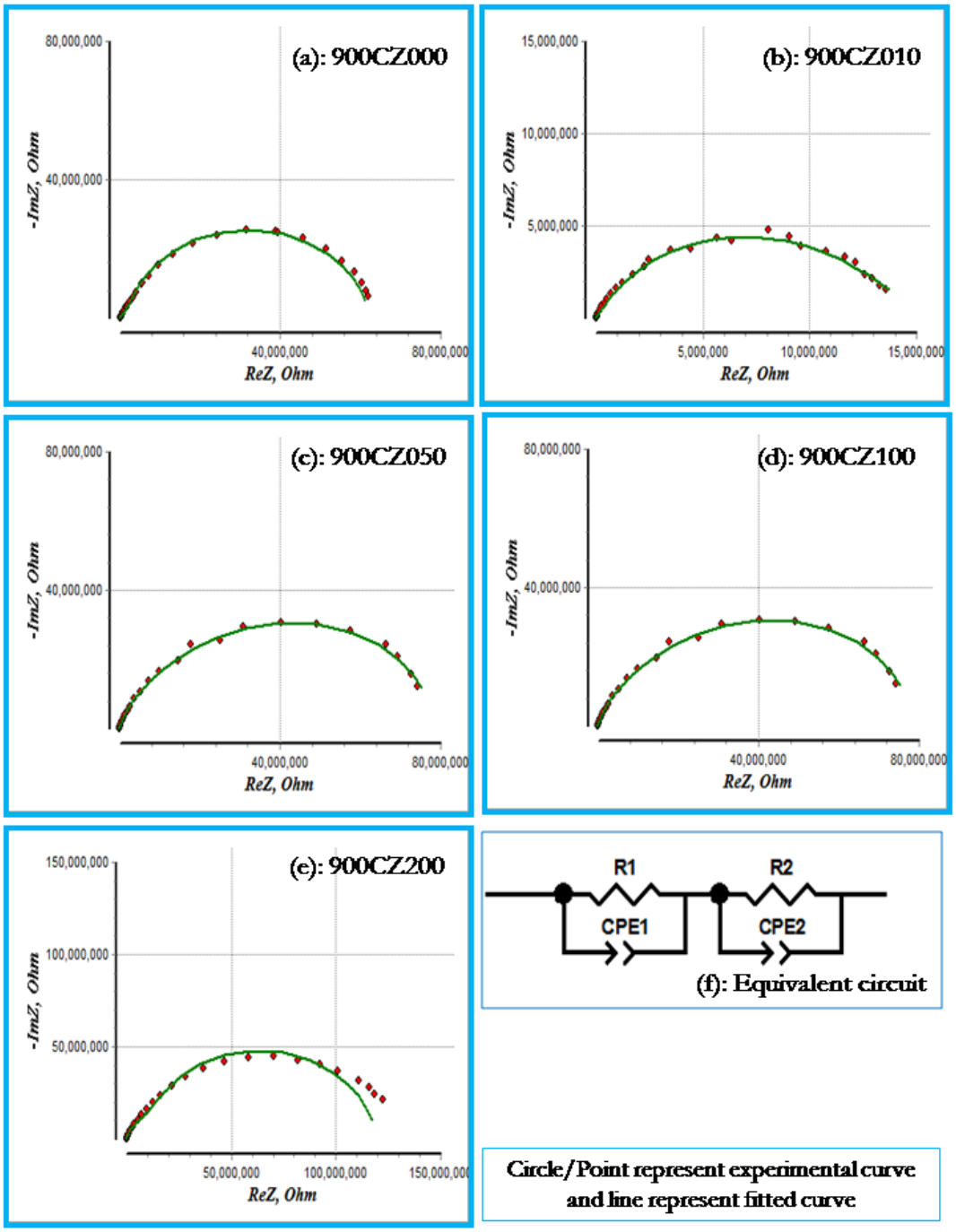

Figure 7.25: Experimental plots, fitted plots and equivalent circuit for fitting of impedance spectra of the samples as a function of ZrO_2 amount measured at 50 °C: (a) 900CZ000 (0.00 mol% ZrO_2); (b) 900CZ010 (0.10 mol% ZrO_2); (c) 900CZ050 (0.50 mol% ZrO_2); (d) 900CZ100 (1.00 mol% ZrO_2), (e) 900CZ200 (2.00 mol% ZrO_2) & (f) equivalent circuit.

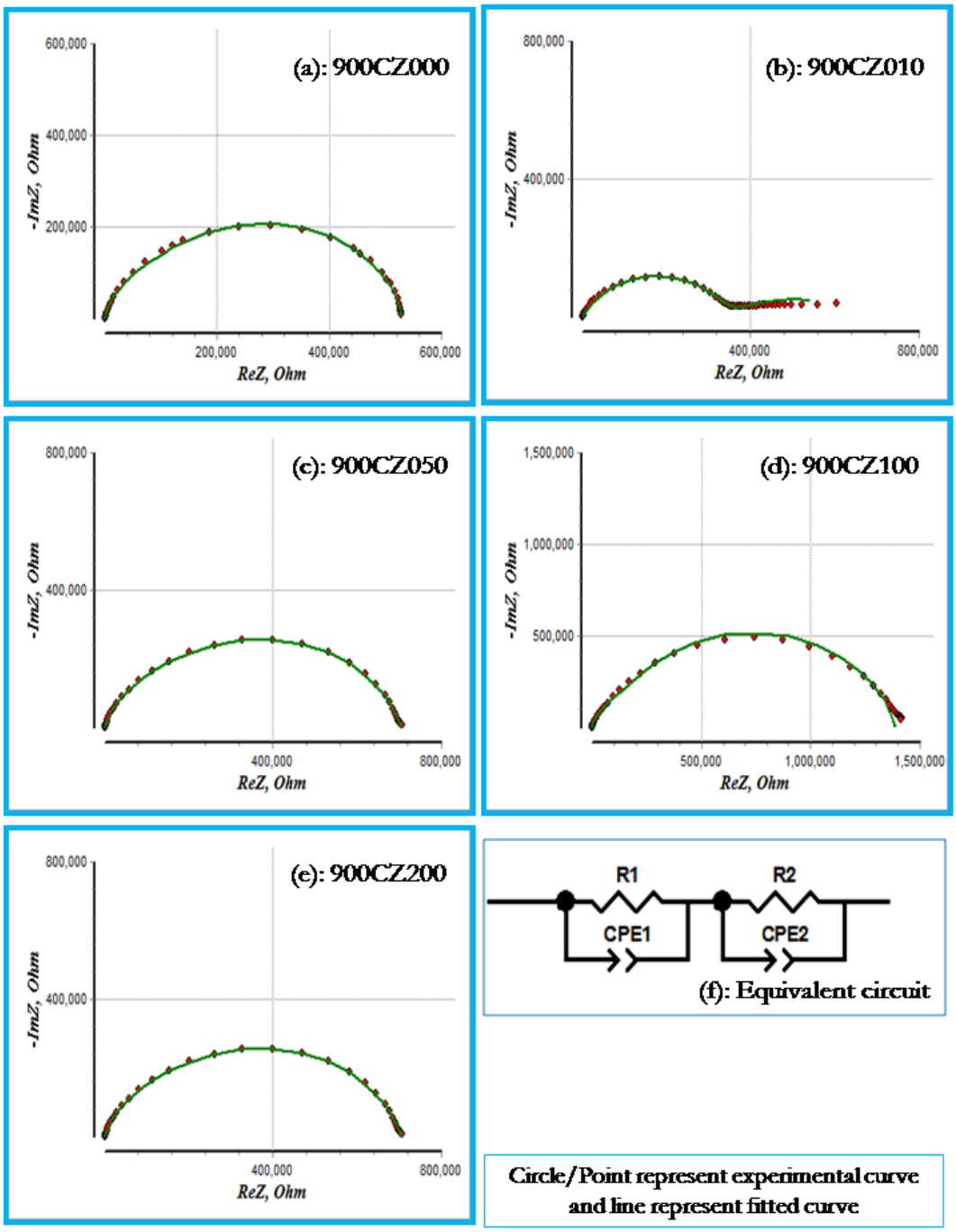

Figure 7.26 Experimental plots, fitted plots and equivalent circuit for fitting of impedance spectra of the samples as a function of ZrO_2 amount measured at 150 °C: (a) 900CZ000 (0.00 mol% ZrO_2); (b) 900CZ010 (0.10 mol% ZrO_2); (c) 900CZ050 (0.50 mol% ZrO_2); (d) 900CZ100 (1.00 mol% ZrO_2), (e) 900CZ200 (2.00 mol% ZrO_2) & (f) equivalent circuit.

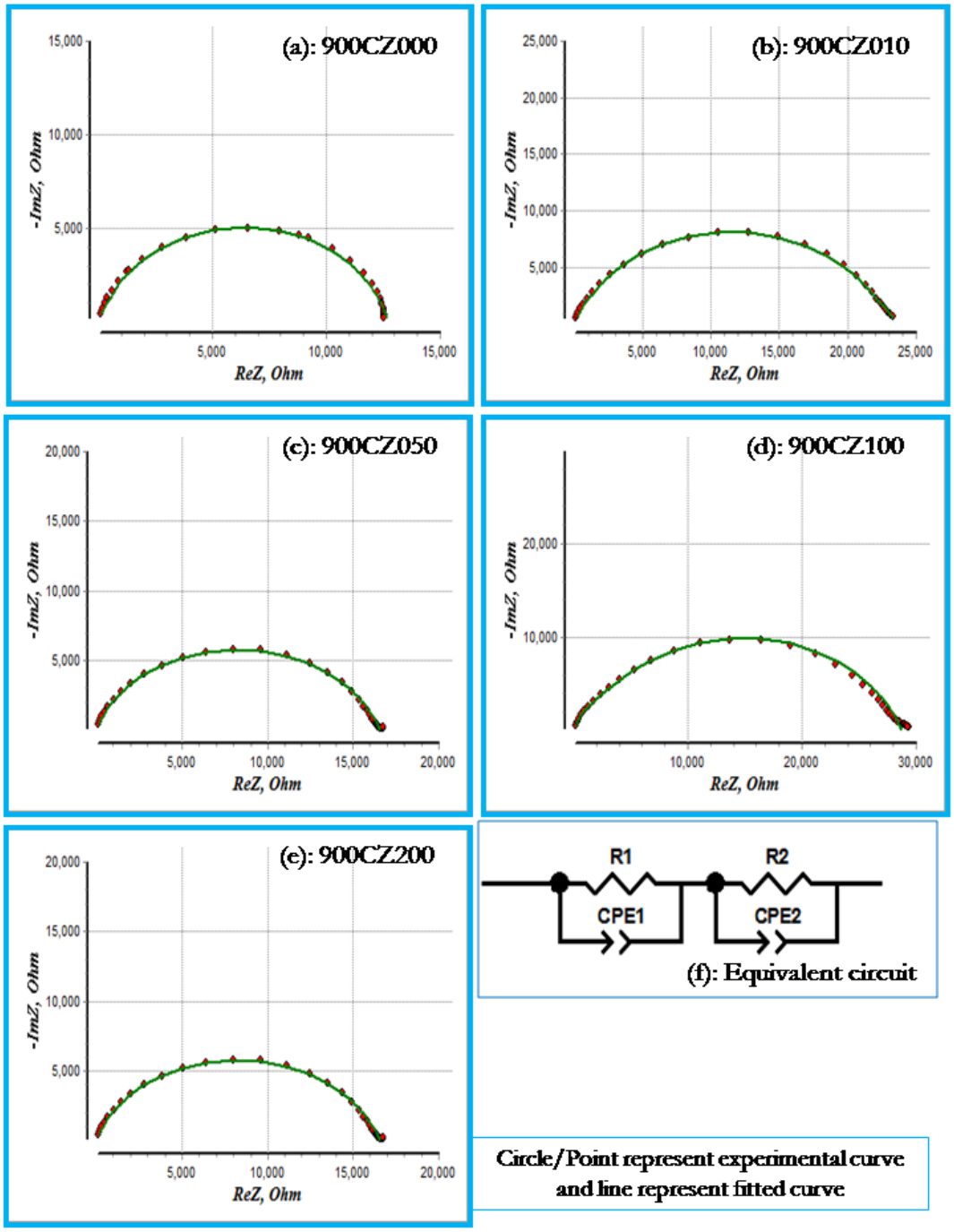

Figure 7.27: Experimental plots, fitted plots and equivalent circuit for fitting of impedance spectra of the samples as a function of ZrO_2 amount measured at 250°C: (a) 900CZ000 (0.00 mol% ZrO_2); (b) 900CZ010 (0.10 mol% ZrO_2); (c) 900CZ050 (0.50 mol% ZrO_2); (d) 900CZ100 (1.00 mol% ZrO_2), (e) 900CZ200 (2.00 mol% ZrO_2) & (f) equivalent circuit.

The resistivity of a polycrystalline material decreases with the increase in grain size due to the decrease in the grain boundary number. Therefore, we found that the 2.00 mol% ZrO_2 doped $ZnO–V_2O_5–Cr_2O_3$ sample has a higher value of resistance among all the samples sintered at 900 °C.

Table 7.13: Summary of fitted electrical parameter obtained from EIS software measured at 50 °C for ZrO_2 doped samples sintered at 900 °C.

Samples (at 50 °C)	R_1 (Ω)	P_1	n_1	R_2 (Ω)	P_2	n_2	R_T (Ω)
900CZ000	1.37×10^6	1.8×10^{-9}	0.91	6.12×10^7	2.2×10^{-9}	0.89	6.26×10^7
900CZ010	1.39×10^6	1.41×10^{-9}	0.88	1.18×10^7	2.5×10^{-9}	0.86	1.32×10^7
900CZ050	4.62×10^6	1.41×10^{-9}	0.92	7.21×10^7	1.3×10^{-9}	0.91	7.68×10^7
900CZ100	8.57×10^6	8.32×10^{-9}	0.93	1.11×10^8	1.3×10^{-9}	0.90	1.20×10^8
900CZ200	1.12×10^7	7.54×10^{-10}	0.93	1.06×10^8	9.7×10^{-10}	0.92	1.17×10^8

Table 7.14: Summary of fitted electrical parameter obtained from EIS software measured at 150 °C for ZrO_2 doped samples sintered at 900 °C.

Samples (at 150 °C)	R_1 (Ω)	P_1	n_1	R_2 (Ω)	P_2	n_2	R_T (Ω)
900CZ000	7.84×10^4	2.38×10^{-9}	0.91	4.52×10^5	2.36×10^{-9}	0.90	5.31×10^5
900CZ010	5.34×10^4	1.88×10^{-9}	0.90	2.84×10^5	3.20×10^{-9}	0.86	3.38×10^5
900CZ050	9.51×10^4	1.85×10^{-9}	0.92	6.04×10^5	2.61×10^{-9}	0.88	6.99×10^5
900CZ100	1.10×10^5	1.36×10^{-9}	0.93	1.28×10^6	2.75×10^{-9}	0.86	1.39×10^6
900CZ200	1.29×10^5	1.22×10^{-9}	0.93	6.95×10^5	2.11×10^{-9}	0.88	8.24×10^5

Table 7.15: Summary of fitted electrical parameter obtained from EIS software measured at 250 °C for ZrO_2 doped samples sintered at 900 °C.

Samples (at 250 °C)	R_1 (Ω)	P_1	n_1	R_2 (Ω)	P_2	n_2	R_T (Ω)
900CZ000	3.60×10^3	3.15×10^{-9}	0.91	9.05×10^3	3.99×10^{-9}	0.90	1.26×10^4
900CZ010	2.11×10^3	2.12×10^{-9}	0.95	2.09×10^4	5.63×10^{-9}	0.82	2.30×10^4
900CZ050	2.09×10^3	2.58×10^{-9}	0.95	1.44×10^4	7.68×10^{-9}	0.83	1.65×10^4
900CZ100	1.24×10^3	1.34×10^{-9}	1.00	2.75×10^4	9.62×10^{-9}	0.79	2.87×10^4
900CZ200	7.03×10^3	2.48×10^{-9}	0.91	2.43×10^4	7.35×10^{-9}	0.82	3.14×10^4

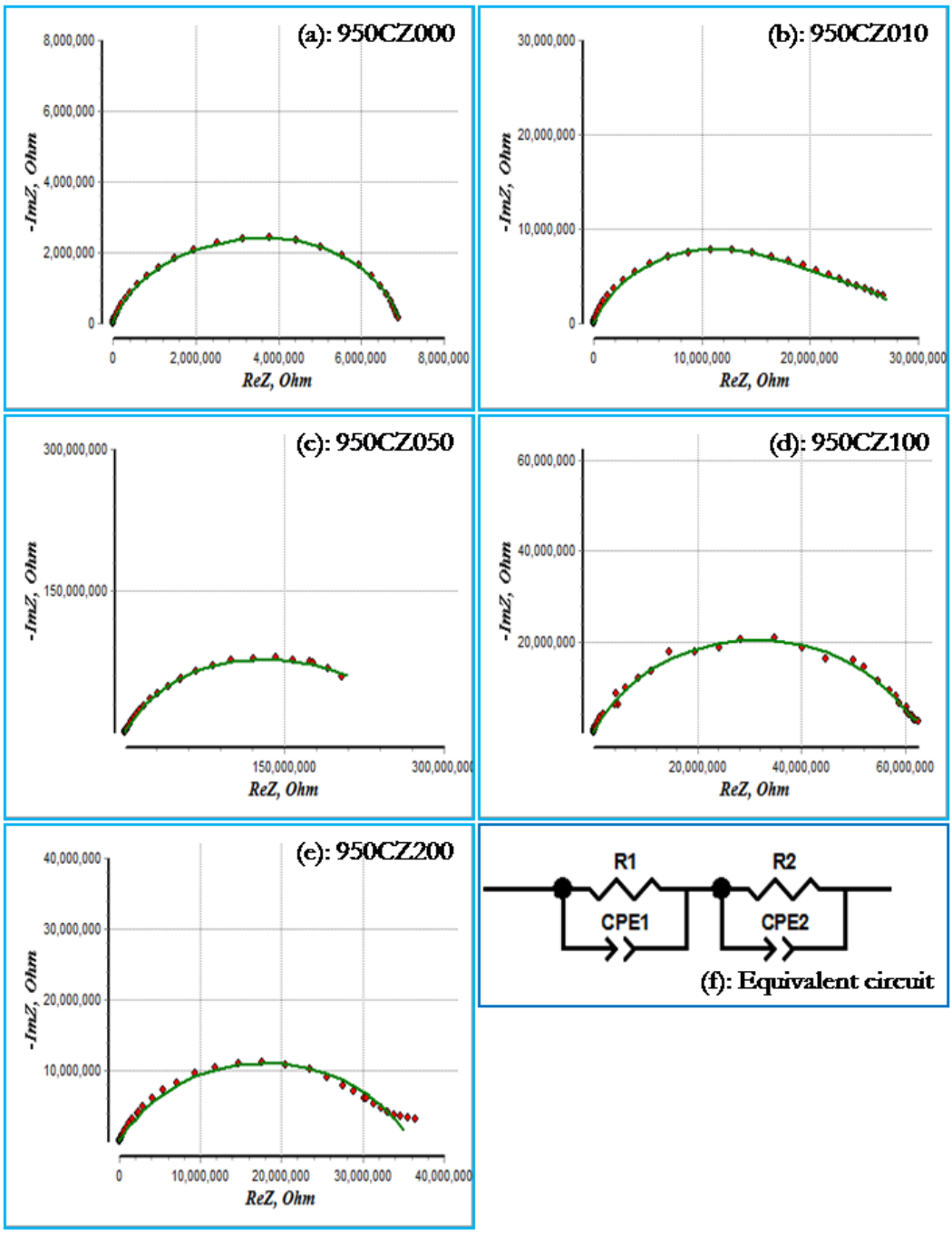

Figure 7.28: Experimental plots, fitted plots and equivalent circuit for fitting of impedance spectra of the samples as a function of ZrO_2 amount measured at 50 °C: (a) 950CZ000 (0.00 mol% ZrO_2); (b) 950CZ010 (0.10 mol% ZrO_2); (c) 950CZ050 (0.50 mol% ZrO_2); (d) 950CZ100 (1.00 mol% ZrO_2), (e) 950CZ200 (2.00 mol% ZrO_2) and (f) equivalent circuit.

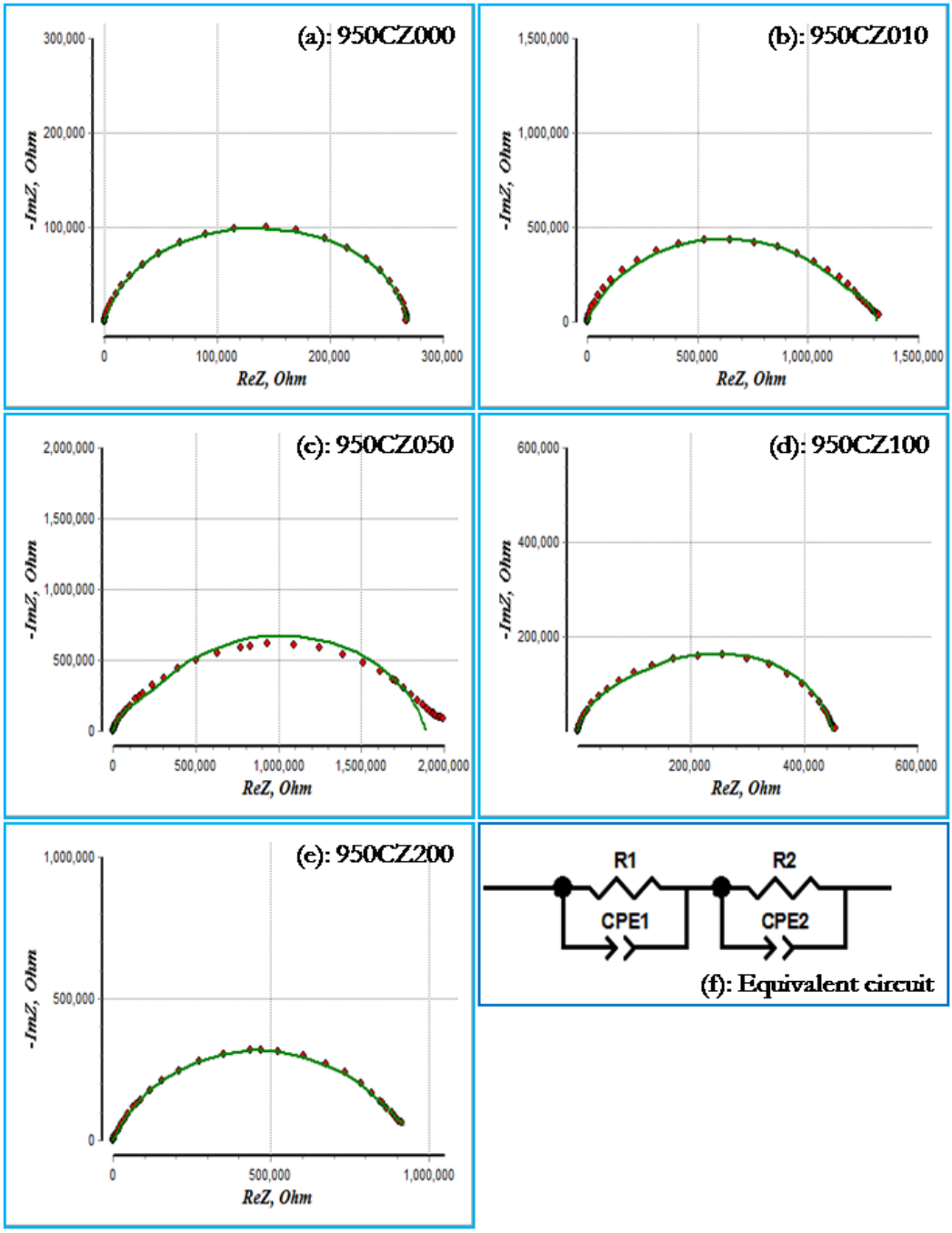

Figure 7.29: Experimental plots, fitted plots and equivalent circuit for fitting of impedance spectra of the samples as a function of ZrO_2 amount measured at 150 °C: (a) 950CZ000 (0.00 mol% ZrO_2); (b) 950CZ010 (0.10 mol% ZrO_2); (c) 950CZ050 (0.50 mol% ZrO_2); (d) 950CZ100 (1.00 mol% ZrO_2), (e) 950CZ200 (2.00 mol% ZrO_2) and (f) equivalent circuit.

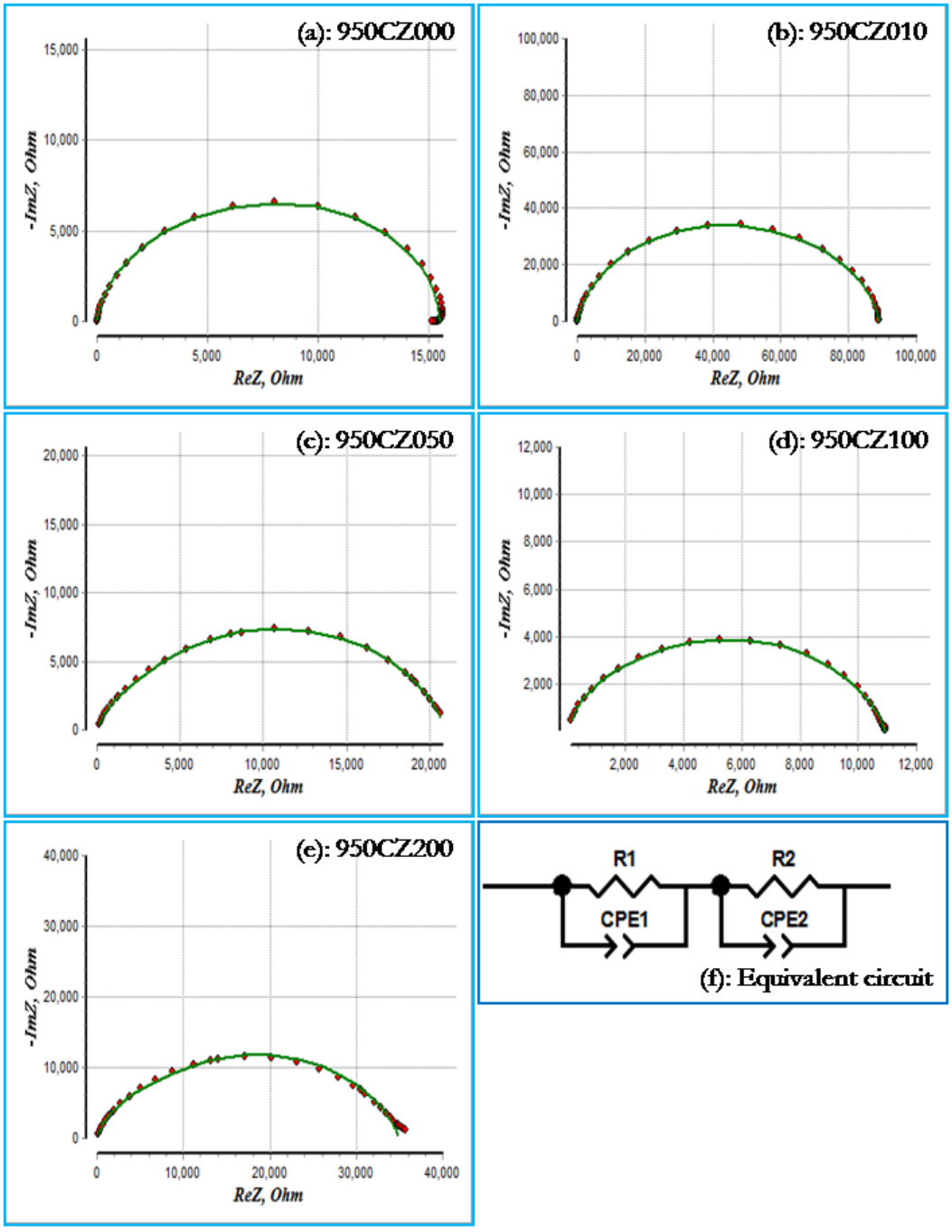

Figure 7.30: Experimental plots, fitted plots and equivalent circuit for fitting of impedance spectra of the samples as a function of ZrO_2 amount measured at 250 °C: (a) 950CZ000 (0.00 mol% ZrO_2); (b) 950CZ010 (0.10 mol% ZrO_2); (c) 950CZ050 (0.50 mol% ZrO_2); (d) 950CZ100 (1.00 mol% ZrO_2), (e) 950CZ200 (2.00 mol% ZrO_2) and (f) equivalent circuit.

Figs. 7.28, 7.29, 7.30 and Tables 7.16, 7.17 & 7.18 shows the total resistance given by R_T (Ω) = R_1 (Ω) + R_2 (Ω) measured at 50 °C, 150 °C & 250 °C of the samples sintered at 950 °C with different amounts of ZrO_2. The R_T (Ω) for the the 0.00, 0.10, 0.50, 1.00 and 2.00 mol% ZrO_2 doped $ZnO–V_2O_5–Cr_2O_3$ samples measured at 50 °C are 6.49 x10^6, 2.99 x10^7, 2.19 x10^8, 5.94 x10^7, 3.55 x10^7 Ω; at 150 °C are 2.60 x10^5, 1.34 x10^6, 1.89 x10^6, 4.51 x10^5, 8.93 x10^5 Ω and at 250 °C are 1.53 x10^4, 8.97 x10^4, 3.50 x10^4, 1.09 x10^4, 2.10 x10^4 Ω respectively. The 0.50 mol% ZrO_2 doped $ZnO–V_2O_5–Cr_2O_3$ sample sintered at 950 °C have a higher value of resistance among all the samples sintered at 950 °C. Since, the resistivity of a polycrystalline material decreases with the increase in grain size and the decrease in the grain boundary number.

Table 7.16: Summary of fitted electrical parameter obtained from EIS software measured at 50 °C for the samples sintered at 950 °C.

Samples (at 50°C)	R_1(Ω)	P_1	n_1	R_2(Ω)	P_2	n_2	R_T(Ω)
950CZ000	5.91 x10^5	8.19 x10^{-10}	1.00	5.90 x10^6	1.8 x10^{-9}	0.99	6.49 x10^6
950CZ010	8.55 x10^6	2.81 x10^{-8}	0.81	2.13 x10^7	7.1 x10^{-10}	0.81	2.99 x10^7
950CZ050	2.01 x10^7	1.68 x10^{-9}	0.85	1.99 x10^8	3.0 x10^{-9}	0.88	2.19 x10^8
950CZ100	5.80 x10^6	9.72 x10^{-10}	0.93	5.36 x10^7	7.6 x10^{-8}	0.89	5.94 x10^7
950CZ200	1.27 x10^5	1.29 x10^{-9}	1.00	3.54 x10^7	2.9 x10^{-9}	0.84	3.55 x10^7

Table 7.17: Summary of fitted electrical parameter obtained from EIS software measured at 150 °C for the samples sintered at 950 °C.

Samples (at 150°C)	R_1(Ω)	P_1	n_1	R_2(Ω)	P_2	n_2	R_T(Ω)
950CZ000	3.73 x10^4	1.04 x10^{-9}	1.00	2.23 x10^5	1.74 x10^{-9}	0.99	2.60 x10^5
950CZ010	3.82 x10^5	1.26 x10^{-8}	0.80	9.53 x10^5	6.19 x10^{-10}	0.86	1.34 x10^6
950CZ050	1.81 x10^5	1.43 x10^{-9}	0.91	1.71 x10^6	3.55 x10^{-9}	0.84	1.89 x10^6
950CZ100	8.89 x10^4	1.48 x10^{-9}	0.92	3.62 x10^5	2.81 x10^{-9}	0.89	4.51 x10^5
950CZ200	1.32 x10^4	2.49 x10^{-9}	0.95	8.80 x10^5	5.23 x10^{-9}	0.82	8.93 x10^5

Table 7.18: Summary of fitted electrical parameter obtained from EIS software measured at 250 °C for the samples sintered at 950 °C.

Samples (at 250°C)	$R_1(\Omega)$	P_1	n_1	$R_2(\Omega)$	P_2	n_2	$R_T(\Omega)$
950CZ000	4.71×10^3	1.20×10^{-9}	1.00	1.06×10^4	3.20×10^{-9}	1.00	1.53×10^4
950CZ010	2.85×10^4	2.96×10^{-9}	0.91	6.12×10^4	5.17×10^{-10}	0.88	8.97×10^4
950CZ050	4.35×10^3	2.94×10^{-9}	0.91	3.07×10^4	8.30×10^{-9}	0.80	3.50×10^4
950CZ100	3.20×10^3	6.10×10^{-9}	1.00	7.67×10^3	7.80×10^{-8}	0.85	1.09×10^4
950CZ200	1.37×10^3	5.32×10^{-9}	0.91	1.96×10^4	1.00×10^{-8}	0.81	2.10×10^4

Figs. 7.31, 7.32 and 7.33 (a-e) present the Arrhenius plots of the R_1 and R_2 regions for high and low frequencies respectively. These figures show the presence of two linear regions with different slopes. The slope change in the two cases occured at ~150 °C. Table 7.19, 7.20 and 7.21 presents the activation energies for the two processes as a function of ZrO_2 doped $ZnO–V_2O_5–Cr_2O_3$ samples calculated from the data presented in Figs. 7.31, 7.32 and 7.33. The resistance data in both R_1 and R_2 regions follow the Arrhenius law [Pandey et al. (2007)]

$$R = R_0 \exp\left(-\frac{E_a}{RT}\right) \tag{7.4}$$

where E_a is the activation energy for conduction, k_B is the Boltzmann's constant and R_0 is the pre-exponential factor. The least square fitting method of the resistance data were used to calculate the activation energies 'Ea' of conduction. The temperature dependence of the R_1 and R_2 regions shows considerable complexity.

Fig. 7.31 shows the curvature in the Arrhenius plots and activation energy in the range of 0.304 to 0.523 eV below approximately 150 °C. This level is related to the charge state of interstitial oxygen $O_i^{-1}$and O_i^0. Above 150 °C, the activation energies were found in the range of 0.403 to 0.736 eV, this is because of the varistor action is critically dependent on the presence of excess oxygen (as well as V) at ZnO-ZnO interfaces and the activation energies with varying temperature. Form Table 7.19, for the 0.00, 0.10, 0.50, 1.00 and 2.00 mol% ZrO_2

doped ZnO–V_2O_5–Cr_2O_3 samples sintered at 850 °C for 3 h, the Ea values are 0.304, 0.400, 0.419, 0.490 and 0.403 eV for R_1 and 0.354, 0.360, 0.463, 0.523 and 0.454 eV for R_2 grain boundaries regions respectively. In relation to the nature of the interface states, two types of grain boundary junctions have been suggested, ZnO–ZnO homojunction (0.304 to 0.523 eV) and ZnO-V_2O_5-ZnO heterojunction (0.403 to 0.736 eV eV) as defined by impedance spectroscopy [West et al. (1997)]. It is quite possible that the compositions of the V rich intergranular phases responsible for the interface states in ZnO varistors are varied with doping constituents and heat-treatment conditions. Consequently, it is reasonable to assign an energy level 0.304 to 0.523 eV to the interface state of ZnO-intergranular phase heterojunction modified by Zr.

Fig. 7.32 shows the curvature in the Arrhenius plots and activation energy in the range of 0.271 to 0.758 eV below approximately 150 °C. The level 0.271 to 0.758 eV is related to the charge state of interstitial oxygen $O_i^{-1}$and O_i^0. Above 150 °C, the activation energies were in the range of 0.508 to 0.758 eV, this is because of the varistor action is critically dependent on the presence of excess oxygen (as well as V) at ZnO-ZnO interfaces and the activation energies with varying temperature. Form Table 7.20, for the 0.00, 0.10, 0.50, 1.00 and 2.00 mol% ZrO_2 doped ZnO–V_2O_5–Cr_2O_3 samples sintered at 900 °C for 3 h, the Ea values below 150 °C for R_1 are 0.271, 0.508, 0.578, 0.758, 0.610 eV and 0.450, 0.519, 0.683, 0.732, 0.682 eV for R_2 grain boundaries regions respectively. In relation to the nature of the interface states, two types of grain boundary junctions have been suggested that is ZnO–ZnO homojunction (0.271 to 0.758 eV) and ZnO-V_2O_5-ZnO heterojunction (0.508 to 0.758 eV), as defined by impedance spectroscopy [West et al. (1997)]. It is quite possible that the compositions of the V-rich intergranular phases responsible for the interface states in ZnO varistors are varied with doping constituents and heat-treatment conditions. Consequently, it is reasonable to assign an energy level 0.271 to 0.758 eV to the interface state of ZnO intergranular phase heterojunction modified by Zr.

Fig. 7.33 shows the curvature in the Arrhenius plots and activation energy in the range of 0.256 to 0.649 eV below approximately 150 °C. This is related to the charge state of interstitial oxygen O_i^{-1} and O_i^0. Above 150 °C, the activation energies were in the range of 0.443 to 0.829 eV, this is because of the varistor action is critically dependent on the presence of excess oxygen (as well as V) at ZnO-ZnO interfaces and the activation energies with varying temperature. Form Table 7.21, for the 0.00, 0.10, 0.50, 1.00 and 2.00 mol% ZrO_2 doped ZnO–V_2O_5–Cr_2O_3 samples sintered at 950°C for 3 h, the Ea values below 150°C are 0.338, 0.363, 0.553, 0.564, 0.256 eV for R_1 and 0.371, 0.372, 0.565, 0.649, 0.448 eV for R_2 grain boundaries regions respectively. In relation to the nature of the interface states, two types of grain boundary junctions have been suggested that is ZnO–ZnO homojunction (0.256 to 0.649 eV) and ZnO-V_2O_5-ZnO heterojunction (0.443 to 0.829 eV), as defined by impedance spectroscopy [West et al. (1997)]. It is quite possible that the compositions of the V-rich intergranular phases responsible for the interface states in ZnO varistors are varied with doping constituents and heat-treatment conditions. Consequently, it is reasonable to assign an energy level of 0.256 to 0.649 eV to the interface state of ZnOintergranular phase heterojunction modified by Zr.

From Arrhenius plots, it is observed that the curve for ZrO_2 doped ZnO–V_2O_5–Cr_2O_3 samples have low temperature region and high temperature region. The change in slope of the graph, from one region to other region occurs between two temperatures, depending upon the sintering temperature as well as the amount of ZrO_2 doped ZnO–V_2O_5–Cr_2O_3 samples. The transition temperatures for the 0.00, 0.10, 0.50, 1.00 and 2.00 mol% ZrO_2 doped ZnO–V_2O_5–Cr_2O_3 samples is approximately 150˚C. The effect of ZrO_2 on the electrical properties of ZnO based resistors can be commentated with grain boundary barrier model for ZnO based resistors. The defects generated by the presence of ZrO_2 as +4 are fundamental in the formation of depletion layers at the grain boundaries in that they lead to the creation of potential barriers when compensated by the negative charges at the grain boundary interface.

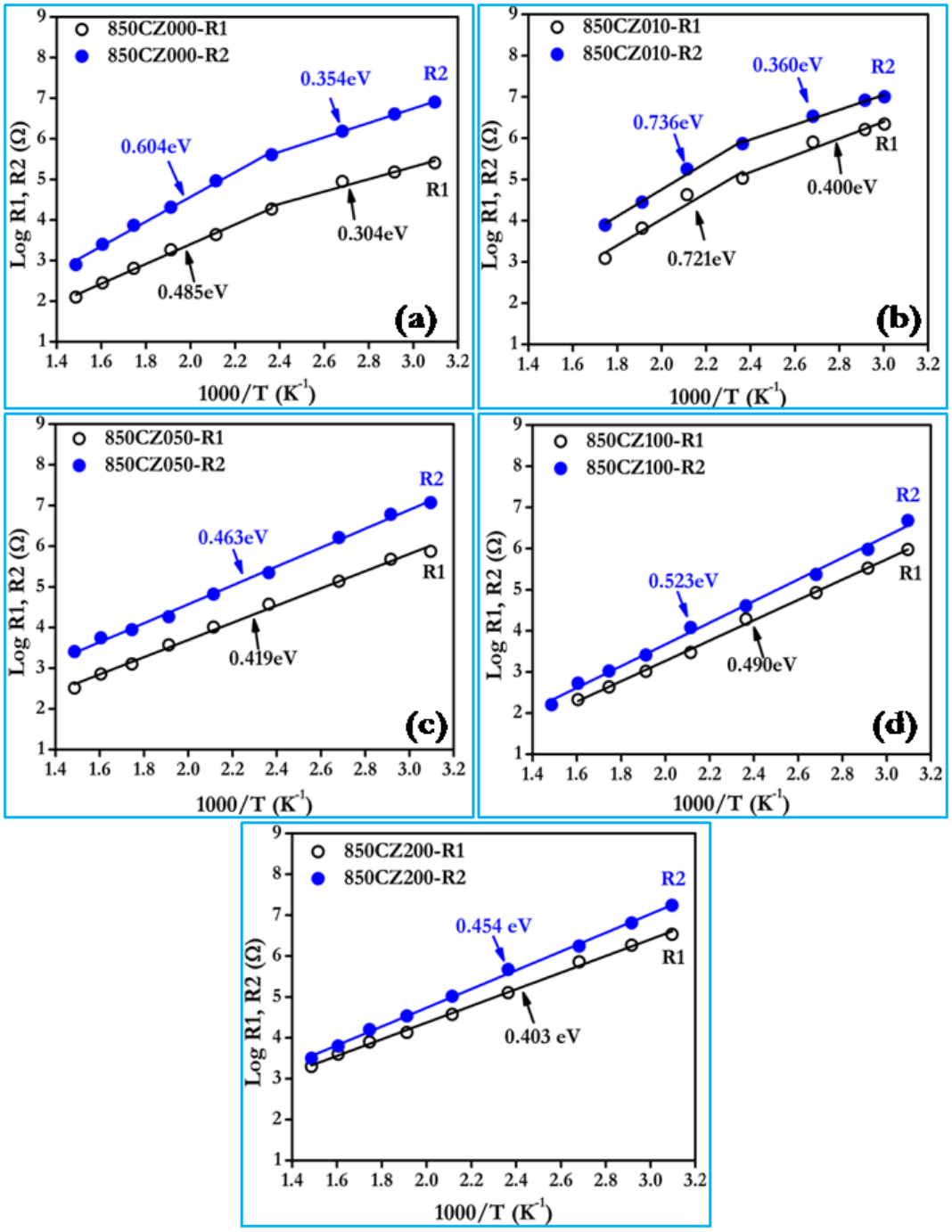

Figure 7.31: Arrhenius plots for resistance R_1 and R_2 associated with low and high frequency grain boundary respectively of the samples as a function of ZrO_2 amount: : (a) 850CZ000 (0.00 mol% ZrO_2); (b) 850CZ010 (0.10 mol% ZrO_2); (c) 850CZ050 (0.50 mol% ZrO_2); (d) 850CZ100 (1.00 mol% ZrO_2) and (e) 850CZ200 (2.00 mol% ZrO_2).

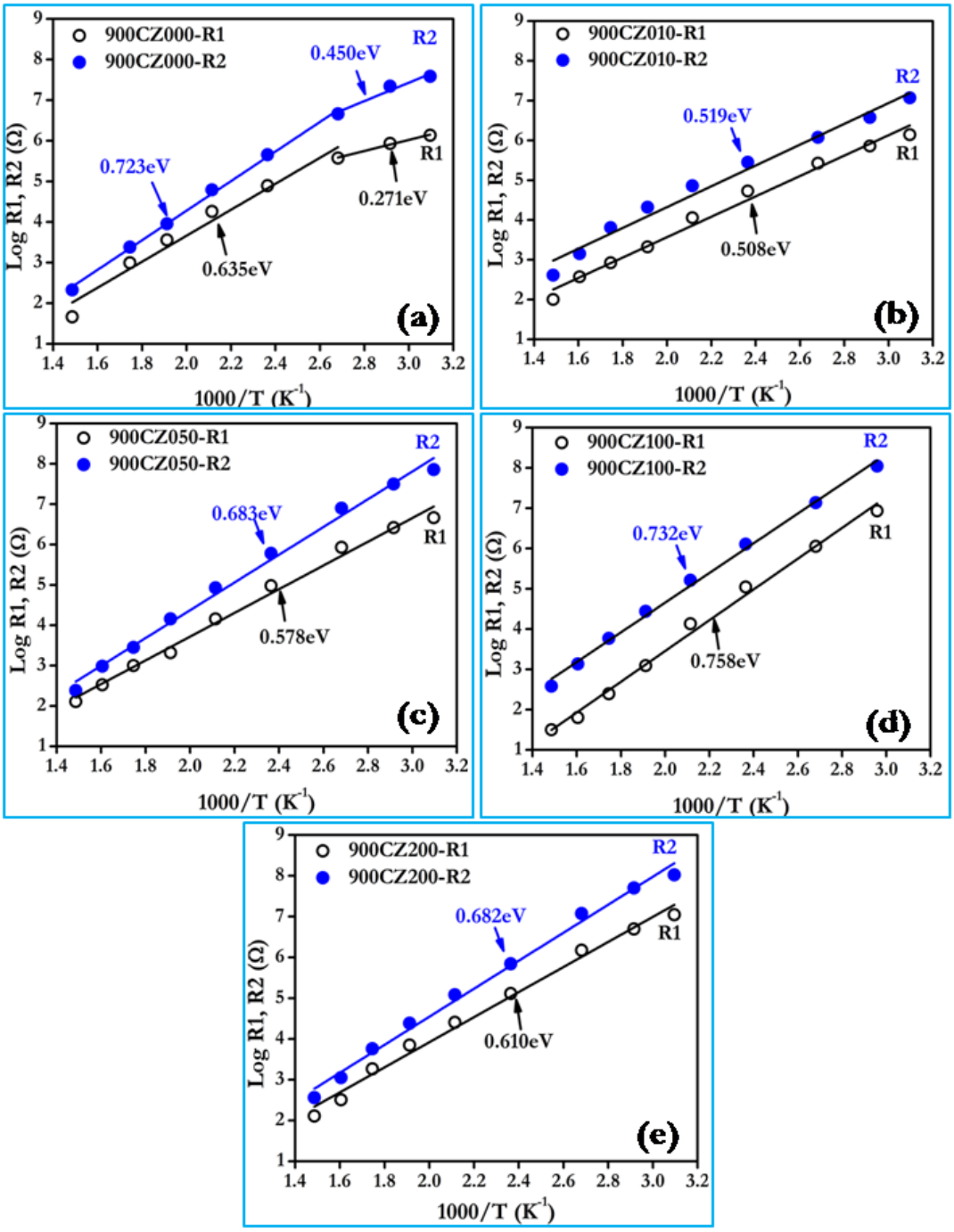

Figure 7.32: Arrhenius plots for resistance R_1 and R_2 associated with low and high frequency grain boundary respectively of the samples as a function of ZrO_2 amount: (a) 900CZ000 (0.00 mol% ZrO_2); (b) 900CZ010 (0.10 mol% ZrO_2); (c) 900CZ050 (0.50 mol% ZrO_2); (d) 900CZ100 (1.00 mol% ZrO_2) and (e) 900CZ200 (2.00 mol% ZrO_2).

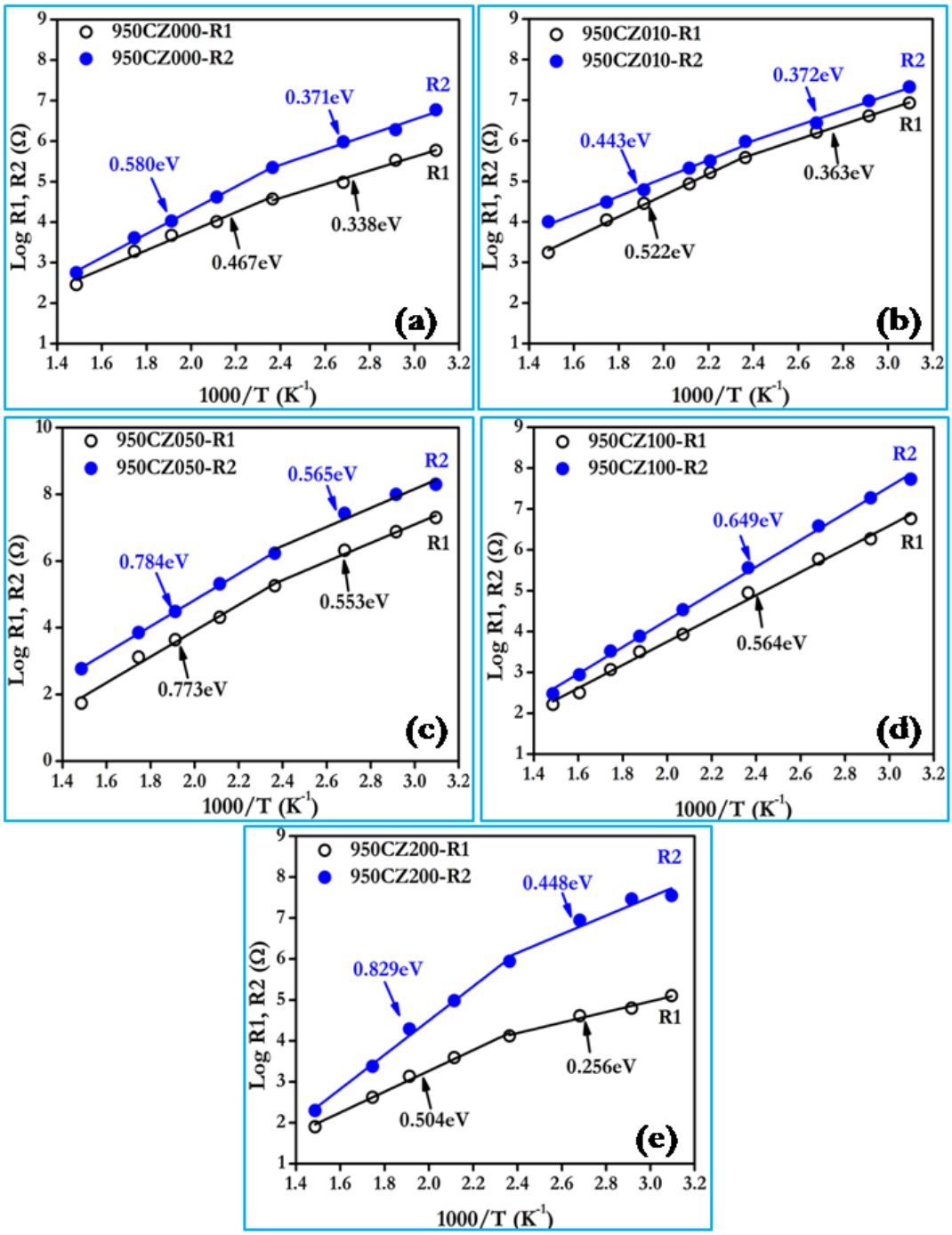

Figure 7.33: Arrhenius plots for resistance R_1 and R_2 associated with low and high frequency grain boundary respectively of the samples as a function of ZrO_2 amount: (a) 950CZ000 (0.00 mol% ZrO_2); (b) 950CZ010 (0.10 mol% ZrO_2); (c) 950CZ050 (0.50 mol% ZrO_2); (d) 950CZ100 (1.00 mol% ZrO_2) and (e) 950CZ200 (2.00 mol% ZrO_2).

Table 7.19: Activation energies calculated from the Arrhenius plot at low and high frequency region for the temperature range below and above 150 °C for the samples sintered at 850 °C.

Samples	R_1 : E_1: (eV)		R_2 : E_2: (eV)	
	T<150 °C	T>150 °C	T<150 °C	T>150 °C
850CZ000	0.304	0.485	0.354	0.604
850CZ010	0.400	0.721	0.360	0.736
850CZ050	0.419	0.419	0.463	0.463
850CZ100	0.490	0.490	0.523	0.523
850CZ200	0.403	0.403	0.454	0.454

Table 7.20: Activation energies calculated from the Arrhenius plot at low and high frequency region for the temperature range below and above 150°C for the samples sintered at 900 °C.

Samples	R_1 : E_1: (eV)		R_2 : E_2: (eV)	
	T<150 °C	T>150 °C	T<150 °C	T>150 °C
900CZ000	0.271	0.635	0.450	0.723
900CZ010	0.508	0.508	0.519	0.519
900CZ050	0.578	0.578	0.683	0.683
900CZ100	0.758	0.758	0.732	0.732
900CZ200	0.610	0.610	0.682	0.682

Table 7.21: Activation energies calculated from the Arrhenius plot at low and high frequency region for the temperature range below and above 150°C for the samples sintered at 950 °C.

Samples	R_1 : E_1: (eV)		R_2 : E_2: (eV)	
	T<150 °C	T>150 °C	T<150 °C	T>150 °C
950CZ000	0.338	0.467	0.371	0.580
950CZ010	0.363	0.522	0.372	0.443
950CZ050	0.553	0.773	0.565	0.784
950CZ100	0.564	0.564	0.649	0.649
950CZ200	0.256	0.504	0.448	0.829

From the Figs. 7.31, 7.32 and 7.33, it is observed that there is a decrease in resistance with increasing temperature. It could be attributed to negative temperature coefficient of resistance and semiconducting behavior of ZrO_2 doped ZnO–V_2O_5–Cr_2O_3 samples, obeying $R=R_0\, e^{-Ea/KT}$ in the temperature range of 50 to 400˚C. The resistance of Zr doped ZnO varistor falls suddenly in linear

fashion up to certain transition temperature and after that the resistance decreases exponentially with increasing temperature. The transition temperature depends on doping concentration as well as sintering temperature.

ZnO is well known for its non-stoichiometry due to the zinc atoms interstitial sites and exhibits oxygen vacancies. These defects introduce donor states in the forbidden band, slightly below the conducting band. The donors are assumed to be interstitial zinc ions Zn^{i}. Using Kroger–Vink notation, we can write:

$$Zn_i^x \rightarrow e' + Zn_i^0 \tag{7.5}$$

$$Zn_i^0 \rightarrow e' + Zn_i^{00} \tag{7.6}$$

where Zn_i^0 and Zn_i^{00} are once and twice ionized interstitial zinc atoms, respectively. Such free electrons (e') moves to the conducting band and enhances the ZnO conductivity which can be further increased by the extrinsic defects. But when ZnO is doped with V_2O_5, a part of the V_2O_5 additive have dissolved into the ZnO matrix and V^{5+} ions enter the interstitial sites of ZnO structure. Therefore, a substitutional reaction was believed to occur as below:

$$V_2O_5 \xrightarrow{ZnO} 2V_{Zn}^{000} + 2O_0 + \frac{3}{2}O_2 + 6e' \tag{7.7}$$

or

$$V_2O_5 \xrightarrow{ZnO} 2V_{Zn}^{000} + 2V_{Zn}^{2} + 5O_0 \tag{7.8}$$

Eq. (7.7) is an electron compensation reaction and the Eq. (7.8) is a defect compensation reaction. As there are more donors induced in ZnO–V_2O_5 than the intrinsic ones in ZnO, the electron compensation reaction seems more likely to have occurred. V_{Zn} is vanadium atom in zinc atom substitution site. In Zn substitutions with Vanadium atoms, free electrons are released and raise the conductivity by increasing electron density. Thus increase in conductivity was observed with increase in V_2O_5 content. Moreover, the zinc vacancies distribute preferably near the grain boundaries for a relaxation of the high strain induced by the vacancies. A schottky barrier might be induced by such a concentration gradient of defects created at the grain boundaries for the ZnO–V_2O_5 system. It should be mentioned that the barrier height depends on the applied voltage and

vanishes above certain field strength. Also the barrier decreases with increase in grain conductivity and collapses when the grain conductivity is too high [Levinson (1979); Hng et al. (1999); (2000)].

Temperature behavior of the impedance data can be described as follows: For lower temperatures, the presence of $V_o^{\cdot\cdot}$ or $Zn_i^{\cdot\cdot}$ may be related with the low and high frequency time constants, respectively. Physically adsorbed water should be ruled out once the varistor system is dense. For higher temperatures, O' and O" are the main adsorbed species at the grain boundary.

Slightly higher values of activation energies for grain boundaries are due to more disordered nature of grain boundaries. Zr can exist in valence states of +4. As a result, more Zr ions were segregated in the grain boundaries and improved the non-linearity characteristics.

Summary: The present chapter discussed the influence of the ZrO_2 doping on the structure and the electrical response of $ZnO–V_2O_5–Cr_2O_3$ based varistors ceramics was analysed using AC impedance spectroscopy. Samples were prepared via solid state reaction at different sintering temperature 850 °C, 900 °C & 950 °C. The microstructure of the ZrO_2 doped $ZnO–V_2O_5–Cr_2O_3$ varistors consisted of ZnO grain as the primary phase, $ZnCr_2O_4$ and $Zn_3(VO_4)_2$ as the major secondary phases, in which $Zn_3(VO_4)_2$ acts as liquid-phase sintering promoter and has a significant effect on the sintered density. The average grain size of the ZrO_2 doped $ZnO–V_2O_5–Cr_2O_3$ system sintered from 850 to 950°C was found to be in range of 1.0 to 4.5 μm, which increases or decreases upon the amount of ZrO_2 addition. Addition of ZrO_2 along with Cr_2O_3 to the binary $ZnO–V_2O_5$ system controlled the abnormal ZnO grain growth and produced a more uniform microstructure. The ZrO_2 doped $ZnO–V_2O_5–Cr_2O_3$ sample sintered at 900°C exhibited the most optimum grain size. EDS spectra of ZnO grain boundary show V, Cr and Zr segregation in the samples. Among all of the samples, the 1.00 mol% ZrO_2-doped sample sintered at 900 °C was found to have the highest values of total resistance of 120 MΩ and exhibited the highest nonlinear coefficient of 19.5, the highest breakdown field value of 662.2 V/mm, the lowest leakage current density of J_L = 120.1 μA/cm^2, the ε' (1KHz) = 218 and the tan δ(1KHz) = 0.293 among all of the samples. Ea values for 1.00 mol% ZrO_2-doped samples sintered at 900 °C were found to be 0.758 and 0.732 eV for the R_1 (high frequency) and R_2 (low frequency) grain boundary regions, respectively. Conclusively, among all of the ZrO_2 doped $ZnO–V_2O_5–Cr_2O_3$ samples, it was found that the 1.00 mol% ZrO_2 doped $ZnO–V_2O_5–Cr_2O_3$ samples sintered at 900 °C is a candidate material for use in chip varistors.

The next chapter gives a salient conclusions derived from the present research work on the effect of different doping on $ZnO–V_2O_5$ based Varistor ceramics sintered at 850 °C, 900 °C and 950 °C presented in the preceding chapter 5 to 7